



Warm mid-Pliocene conditions without high climate sensitivity: the CCSM4-Utrecht (CESM 1.0.5) contribution to the PlioMIP2

Michiel L. J. Baatsen¹, Anna S. von der Heydt^{1,2}, Michael A. Kliphuis¹, Arthur M. Oldeman¹, and Julia E. Weiffenbach¹

¹Institute for Marine and Atmospheric research Utrecht (IMAU), Department of Physics, Utrecht University, Utrecht, The Netherlands.

²Centre for Complex Systems Science, Utrecht University, Utrecht, The Netherlands

Correspondence: Michiel Baatsen (m.l.j.baatsen@uu.nl)

Abstract. We present the Utrecht contribution to the Pliocene Model Intercomparison Project Phase 2 (PlioMIP2), using the Community Earth System Model version 1.0.5 (*CCSM4-Utr*). Using a standard pre-industrial configuration and the *enhanced* PlioMIP2 set of boundary conditions, we perform a set of simulations at various levels of atmospheric pCO₂. This allows us to make an assessment of the mid-Pliocene reference (Eoi⁴⁰⁰) climate versus available proxy records and a pre-industrial control (E²⁸⁰), as well as to determine the sensitivity to different external forcing mechanisms.

We find that our simulated Pliocene climate is considerably warmer than the pre-industrial reference, even under the same levels of atmospheric pCO₂. Compared to the E²⁸⁰ case, the simulated climate of our Eoi⁴⁰⁰ is on average almost 5°C warmer at the surface. Our Eoi⁴⁰⁰ case is among the warmest within the PlioMIP2 ensemble and only comparable to the results of models with a much higher climate sensitivity (i.e. CESM2, EC-Earth3.3, and HadGEM3). This is accompanied by a considerable polar amplification factor, increased precipitation and greatly reduced sea ice cover. A primary contribution to this enhanced Pliocene warmth is likely our warm model initialisation followed by a long spin-up, as opposed to starting from pre-industrial or present-day conditions. Added warmth in the deep ocean is partly the result of using an altered vertical mixing parametrisation in the Pliocene simulations, but this has a negligible effect at the surface. We find a stronger and deeper Atlantic Meridional Overturning Circulation (AMOC) in the Eoi⁴⁰⁰ case, but the associated meridional heat transport is mostly unaffected. In addition to the mean state, we find significant shifts in the behaviour of the dominant modes of variability at annual to decadal timescales. The Eoi⁴⁰⁰ ENSO amplitude is greatly reduced (-68%) versus the E²⁸⁰ one, while the AMOC becomes more variable. There is also a strong coupling between AMOC strength and North Atlantic SST variability in the Eoi⁴⁰⁰, while North Pacific SST anomalies seem to have a reduced global influence with respect to the E²⁸⁰ through the weakened ENSO.



1 Introduction

The Pliocene Model Intercomparison Project Phase 2 (PlioMIP2; Haywood et al. 2016) aims at simulating the mid-Piacenzian Warm Period (mPWP; 3.264 to 3.025 Ma; Haywood et al. 2013a) of the mid-Pliocene using a suite of global numerical climate models. During this interval, the Earth's climate saw warm stable conditions with atmospheric CO₂ levels similar to those seen today. Being relatively recent in the planet's geologic history, geographical boundary conditions during the mid-Piacenzian were similar to the present. Therefore, the simulated climatic conditions for this specific time interval may serve as a suitable analogue of what to expect in the next century (Burke et al., 2018).

Previous modelling efforts within PlioMIP1 resulted in globally averaged near surface air temperatures between 1.8 and 3.6 °C warmer than those seen today (Haywood et al., 2013b), for the mid-Pliocene. The pattern of warming showed clear polar amplification, resulting in a reduced equator-to-pole temperature gradient. However, this reduction was still considerably smaller than suggested by various temperature proxy records and models mostly failed to reproduce the strong warming pattern over the North Atlantic Ocean. The simulated mid-Pliocene warming response was found to be mostly a result of increased atmospheric CO₂, with surface albedo feedbacks the primary driver behind polar amplification.

In addition to an extended model ensemble, PlioMIP2 offers the use of model boundary conditions from the Pliocene Research, Interpretation and Synoptic Mapping version 4 (PRISM4; Dowsett et al. (2016)). This includes updated estimates of vegetation cover, coastlines, and topography as well as reduced ice sheet cover compared to PRISM3 (Dowsett et al., 2010). As a result, models now show an average warming response of 1.7 to 5.2 °C to these mid-Pliocene boundary conditions. In addition, most models have a mid-Pliocene temperature pattern that better resembles that of proxy reconstructions, particularly with warmer high latitude and North Atlantic regions compared to PlioMIP1.

Here, we present the results of a set of simulations using the Community Earth System Model (CESM) version 1.0.5 within the PlioMIP2 effort. A detailed description of our model configuration, as used in these experiments, is provided in Section 2. This is followed by a general discussion of the PlioMIP2 experimental design and naming conventions in Section 3, together with an overview of our specific set of model experiments. The results of these are presented in Section 4, in which we assess climate sensitivity (4.1), the general mPWP conditions in our simulations (4.2), meridional overturning and heat transports (4.3), a comparison to proxy records (4.4), sensitivity to the applied PlioMIP2 model boundary conditions (4.5), and modes of internal variability in the simulated climate (4.6).

2 Model description

2.1 The CESM 1.0.5

The Community Earth System Model (Hurrell et al., 2013) is a fully coupled atmosphere-land-ice-ocean general circulation model (GCM) that was developed at the National Center for Atmospheric Research (NCAR) in Boulder, Colorado. For use in palaeoclimate modelling, version 1.0.5 of the CESM is a suitable choice motivated by a trade-off between increasing model complexity and computational cost. This version of the CESM is equivalent to the latest version of the Community Climate



System Model (CCSM4; Blackmon et al. 2001; Gent et al. 2011). In other PlioMIP2 studies, our model simulations are therefore referred to as *CCSM4-Utr*.

55 2.2 Atmosphere

The atmospheric component of the CESM is the Community Atmosphere Model (CAM4; Neale et al. 2013) which uses a finite volume dynamical core. The model grid has a nominal horizontal resolution of 2° ($2.5^\circ \times 1.9^\circ$; 144×96 grid cells). 26 vertical levels extend upward to 2 hPa, using a hybrid sigma vertical coordinate. In this configuration, the model has a warming response of 3.17°C per doubling of CO_2 starting from pre-industrial conditions (Baatsen et al., 2020), which is very similar to
60 the reported value of 3.14°C by Bitz et al. (2012), and higher than the $\sim 2.5^\circ\text{C}$ in CCSM3; Kiehl et al. 2006).

In accordance to the PlioMIP2 protocol (Haywood et al., 2016), atmospheric concentrations other than that of CO_2 are kept at their pre-industrial levels: 671ppb CH_4 , 270ppb N_2O , and no CFCs. The solar constant is kept at 1361.27 Wm^{-2} in all of our model experiments. Astronomical orbital parameters are set to their present-day configurations for pre-industrial as well as Pliocene simulations, again as suggested by the PlioMIP2 protocol. Atmospheric aerosols are fixed using a pre-industrial
65 climatology, switching to an adjusted Pliocene climatology resulting from a Bulk Aerosol Model simulation to incorporate the effect of the PRISM4 boundary conditions.

2.3 Land

The physical, chemical and biological processes taking place on land are represented in the Community Land Model (CLM4; Oleson et al. 2010; Lawrence et al. 2011). A static rather than dynamic vegetation model is used here to avoid runaway feedback
70 effects, which can become an issue especially in warm greenhouse climates (e.g. dieback of vegetation at low latitudes; Loftson et al. 2014; Herold et al. 2014). Either the pre-industrial biomes or the PRISM4 megabiomes (see also Supplementary Table S1) are translated into fractions of the corresponding CLM4 plant functional types (PFTs), from which a set of monthly forcing files is ultimately used in the model. Fresh water runoff is treated by a simple river routing scheme, in which all runoff is transported to one of the surrounding 8 model grid cells until the ocean is reached. The direction is determined by the local
75 topography gradient and manually adjusted where the runoff scheme would otherwise form closed loops. Within the CLM4, land ice is implemented as bare soil with a given surface elevation and its specific surface properties (e.g. albedo, evaporation and run-off). As suggested by Haywood et al. (2016), the static land ice configuration used here is based on the results of previous modelling efforts in PlioMIP1. This includes a greatly reduced Greenland Ice Sheet compared to the present day, as well as an absent West-Antarctic Ice Sheet.

80 2.4 Ocean

The CESM1 uses the Los Alamos National Laboratory (LANL) Parallel Ocean Program version 2 (POP2; Smith et al. 2010) for the ocean model component. The standard configuration is applied here, with a nominal 1° ($1.25^\circ \times 0.9^\circ$) horizontal resolution on a curvilinear grid placing the northern pole over Greenland. The POP2 model is set up with 60 vertical layers of varying



thickness between 10m near the surface and 250m at greater depth. Horizontal viscosity is considered anisotropic (Smith and
85 McWilliams, 2003) and horizontal tracer diffusion follows the parameterisation of Gent and McWilliams (1990). The model
further uses the KPP-scheme to determine vertical mixing coefficients (Large et al., 1994). More information and discussion
on the ocean model physics and parameterisations can be found in Danabasoglu et al. (2008, 2012).

The sea ice component consists of the LANL Community Ice Code version 4 (CICE4; Hunke and Lipscomb 2008). For
simplicity, sea ice only forms when the sea surface cools down to -1.8°C , after which its dynamical behaviour (e.g. melt and
90 advection) is treated by the model specifically.

In all of our model experiments, tidal mixing and overflow parameterisations are switched off. The pre-industrial reference
uses a uniform background vertical diffusivity, set at $0.16\text{ cm}^2\text{s}^{-1}$. In contrast, the Pliocene simulations have a vertically
varying background vertical diffusivity determined by: $\kappa_w = vdc1 + vdc2 \tan^{-1}(|z| - dpth)linv$, where: $vdc1 = 0.524\text{ cm}^2\text{s}^{-1}$,
 $vdc2 = 0.313\text{ cm}^2\text{s}^{-1}$, $dpth = 1000\text{m}$ (the reference depth) and $linv = 4.5 \cdot 10^{-3}\text{ m}^{-1}$ (the inverse scaling length). κ_w thus varies
95 between $0.1\text{ cm}^2\text{s}^{-1}$ at the surface and $1\text{ cm}^2\text{s}^{-1}$ at the bottom of the ocean. We carry out an additional pre-industrial simulation
with the same oceanic configuration used for the Pliocene cases (see Section 3), to study the effect of these altered parameter
settings compared to the standard configuration (Figures S4 and S8 in the supplementary material). The enhanced vertical
mixing in the deep ocean results in an overall warming of the deep ocean at the expense of a slight cooling at upper levels.
Near the surface, however, very little change is seen as a result of the different vertical mixing schemes. Another pre-industrial
100 simulation in which we turn on the tidal mixing and overflow parameterisations shows that their combined effect is negligible
within the scope of this study and the specific model configuration used here (i.e. no significant temperature differences seen
at any depth level).

3 PlioMIP2 experiments

3.1 PRISM4 boundary conditions

105 Following the methodology outlined by Haywood et al. (2016), we perform a set of pre-industrial and Pliocene simulations
using the CESM1.0.5. As we carry out a number of different model experiments, we will refer to these as either *pre-industrial* or
Pliocene (rather than mid-Piacenzian) regardless of atmospheric pCO_2 . For Pliocene cases we incorporate the set of enhanced
boundary conditions based on the PRISM4 (Dowsett et al., 2016). These include altered topography and bathymetry, coastlines,
land surface properties (i.e. vegetation, soil type and ice sheet coverage) and atmospheric composition with respect to pre-
110 industrial conditions. Our Pliocene model geography is implemented by applying the PRISM4 topography and bathymetry
anomalies to the pre-industrial reference, after re-gridding onto the specific model resolution used here. The PRISM4 land-sea
mask is then also interpolated onto the model grid and applied to the Pliocene model geography. A manual check of the entire
model grid is done, altering land and ocean cells where needed and making sure that any marine passages are either at least 2
cells wide when open, or closed if needed. The resulting model geography for the Pliocene simulations is shown in Figure 1
115 and compared to that of the pre-industrial reference. Corresponding vegetation cover and aerosol optical depth can be found in
Figure S1 of the supplementary material.



Some of the main aspects of the Pliocene model geography with respect to the pre-industrial reference include a closure of

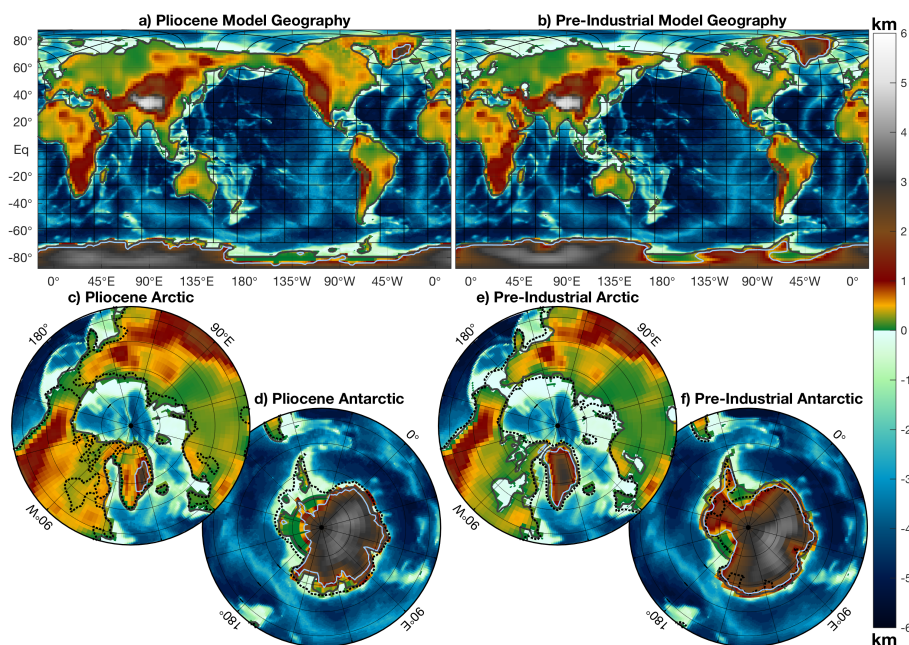


Figure 1. Model geography as applied in our different **a)** Pliocene and **b)** pre-industrial cases. Both the bathymetry and topography are shown at the native model grid, with the CAM4 rectangular grid superimposed on the finer POP2 curvilinear grid wherever the land fraction is at least 0.5 (also indicated by the thick grey contour line). The light blue contour line shows the extent of land ice, as imposed by the land use distribution. **c,e** Northern and **d,f** Southern polar stereographic views Pliocene and pre-industrial model geography.

both the Bering Strait and Northwest Passage, making the Arctic Ocean much more isolated from the other ocean basins. Prior to large-scale glaciation on the Northern Hemisphere during the Quaternary period, a considerable part of the northern
120 Eurasian continental shelf as well as the Hudson Bay area were exposed. Furthermore, large parts of the Maritime Continent are also considered to have been above sea level during the mid-Pliocene. Finally, there was significantly less land ice cover compared to the present, covering only part of Southeast Greenland and East Antarctica. Note that the Gibraltar straight is open while the Panama Gateway is closed in all of our simulations (this is obscured in the figures by the superposition of the atmospheric model grid onto the bathymetry).

125 3.2 Experimental design and model spin-up

In accordance with the PlioMIP2 guidelines we performed both a pre-industrial reference and Pliocene control *core* simulation, which are referred to as E^{280} and Eoi^{400} , respectively (following the naming conventions of Haywood et al. 2016). In addition to the pre-industrial reference we added two *climate sensitivity* simulations, with a doubling (E^{560}) and quadrupling (E^{1120}) of atmospheric CO_2 . Two more sensitivity experiments were added to the Pliocene control, in which we applied pre-industrial
130 (Eoi^{280}) and doubled (Eoi^{560}) CO_2 levels. This enables us to make a complete assessment of the model's sensitivity to either



Pliocene boundary conditions or radiative forcing, for the full range of possible reference states. Besides altered model boundary conditions, the Pliocene simulations differ from the pre-industrial ones as a result of the oceanic vertical mixing parameters. Another *mixing sensitivity* experiment is thus added as a continuation from the E^{280} simulation, using the same ocean mixing configuration for the ocean as in the Pliocene cases, referred to as $E^{280,P}$. Results of an additional (500-year) pre-industrial simulation with tidal mixing and overflow parameterisations switched on ($E^{280,S}$), are not used besides a technical robustness check and therefore not considered. See also Table 1 for an overview of the different simulations.

The pre-industrial reference simulation is initialised using present-day (year 2000) temperature and salinity fields from the

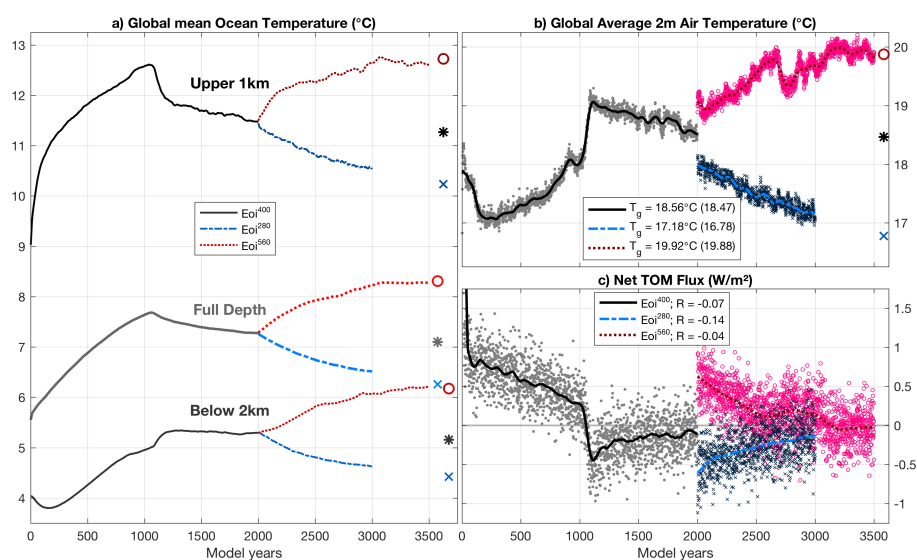


Figure 2. Time series of globally averaged temperatures for the entire length of our 3 different Pliocene simulations: Eoi^{400} (black), Eoi^{280} (blue), and Eoi^{560} (red). Shown are the **a**) upper (dark), deep (medium), and full depth (light) ocean temperature, **b**) near surface air temperature, and **c**) globally averaged top of model (TOM) net radiative flux. Thick lines in b,c show the corresponding time series after applying a 100-year smoothing mask. The estimated equilibrium temperatures are indicated at the end in a,b, using large markers and the same colour convention. The globally averaged, mean temperature (T_g in b) and net radiative flux (R in c) over the last 100 years are added in the legends (bracketed values for the estimated equilibrium).

PHC2 dataset (Steele et al., 2001). As these are slightly warmer than pre-industrial conditions, a long spin-up of >3000 years is carried out to equilibrate the full ocean. The remaining drift of volume-weighted average ocean temperature at the end of this simulation is brought down to $\sim 10^{-4}$ K/year (Table 1). In contrast, the Pliocene control simulation is started with a highly idealised ocean temperature and salinity distribution. The initial temperature is horizontally homogeneous while salinity is set to 35psu globally. The vertical profile of temperature decreases downward between $15^\circ C$ at the surface and $4^\circ C$ in the deep ocean. We thus apply the same initial conditions as those used in the Eocene simulations of Baatsen et al. (2020), with a downward adjustment of deep ocean temperatures. The latter is done to match the volume-integrated, global ocean temperatures of Rosenbloom et al. (2013), who used the CCSM4 to model the mid-Pliocene within the PlioMIP1. This way, we start the model



with a total ocean heat content similar to previously found Pliocene conditions using a very similar model configuration. Still, we perform 2000 model years of spin-up to acquire a well-equilibrated oceanic state for our Pliocene control. An overview of the temperature evolution during this spin up along with the top of model radiative imbalance can be found in Figure 2. Additional information on the spin-up behaviour of the set of model simulations presented here can be found in Figures S2 and S3 of the supplementary material.

All three pre-industrial sensitivity experiments are started from the equilibrated state of the E^{280} control simulation. The E^{560} and E^{1120} cases are continued for another 1000 and 2000 model years, respectively, while the $E^{280,P}$ is continued for 2000 model years (see also Figure S4 of the supplementary material). The E^{560} and E^{1120} simulations still have substantial drifts in deep ocean temperature, but much less near the surface. Using the transient behaviour, however, we can estimate the actual equilibrium temperatures (see section 3.3) and therefore the climate sensitivity of the model within this specific set-up. In the global average, the effect of altered ocean mixing parameters is quite clear: there is no temperature change at the surface, but the upper ocean cools slightly while the deep ocean warms. The more efficient downward mixing of heat leads to an average warming of the total water column (by $\sim 0.8^\circ\text{C}$) in the extrapolated equilibrium. The Eoi^{280} and Eoi^{560} simulations are initialised from the Eoi^{400} control at year 2000 and continued for 1000 and 1500 years, respectively. As their initial radiative forcing is relatively small compared to a full doubling of CO_2 , they acquire a small temperature drift relatively quickly. The Eoi^{560} simulation is longer compared to the Eoi^{280} one as it was showing substantial internal variability after about 700 years owing to large (i.e. $>10\text{Sv}$) fluctuations in the Atlantic Meridional Overturning Circulation strength (see also Figure S5 in the supplementary material).

3.3 Data analysis and methods

Within the PlioMIP2, data from the last 100 model years of the E^{280} , E^{560} , Eoi^{280} , Eoi^{400} , and Eoi^{560} case are publicly available. We use the same 100 years here for our analyses and to calculate time means in order to best match the results of other studies. Some more extensive data time series are considered as well, but only when noted specifically. The overview of modelled atmospheric and oceanic conditions given in Section 4.2 is based on climatologies using the same 100 years at the end of the E^{280} and Eoi^{400} runs. From the $E^{280,P}$ simulation we use 200-year averages instead (i.e. 4400–4600) as it exhibits some long-term fluctuations (see Figure S4 in the supplementary material). In addition to the model data presented here, we make use of the ERSST dataset (Huang et al., 2017), satellite-based passive microwave sea ice concentration data (Peng et al., 2013), and the mid-Pliocene SST proxies from Foley and Dowsett (2019). Pre-industrial SSTs are represented by the 1870–1899 mean SST, which is calculated from the ERSST version 5 monthly fields. We also use the 1988–2000 mean sea ice concentration, excluding more recent years in which a rapid decline of Arctic sea ice was observed.

In addition to direct climatological or annual mean fields, we also present a number of estimated equilibrium values using the complete time series of a particular model run. Based on the method of Gregory et al. (2004), we linearly extrapolate the trend of a specific temperature measure towards a net zero top of model (TOM) radiative flux. It should be noted that the original technique of Gregory et al. (2004) is designed to estimate equilibrium temperatures from relatively short (~ 50 years)



180 simulations following an initial perturbation. Using a much longer time series, we do include the effects of slower feedbacks
such as deep ocean thermal adjustment and therefore can acquire a better estimate of the actual equilibrium temperature (but
also require a much longer simulation time). The net TOM radiation is calculated by subtracting the (surface-weighted) glob-
ally averaged net outgoing longwave flux from the net incoming shortwave flux. A visualisation of the standard procedure
for globally averaged near surface air temperature in the Eoi²⁸⁰, Eoi⁴⁰⁰, and Eoi⁵⁶⁰ cases can be found in Figure S2 of the
185 supplementary material. An extension towards upper (<1km), deep (>2km) and full-depth ocean temperatures from all of our
simulations is also provided in Figure S3. As shown by Gregory et al. (2004), the equilibration of the globally averaged near
surface air temperature from an initial shock in radiative forcing becomes linear as a function of the net TOM radiative flux.
However, their simulations use a slab ocean rather than a full-depth ocean model component. Using our model configuration,
the equilibration is slightly non-linear instead, especially at the start of the simulation (see also Baatsen et al. 2020). Therefore,
190 we exclude the first 100 or 250 years of data from this analysis for atmospheric or oceanic temperatures, respectively.

In our analysis of the ocean circulation, we consider the barotropic stream function (BSF) and meridional overturning stream
function (MSF). Both of these are calculated from the monthly averaged horizontal flow fields and integrated as a function of
latitude and either depth (BSF) or longitude (MSF), starting from the southern pole located on Antarctica. These analyses are
195 again using the last 100 years of model output from each of our simulations. From the MSF, we also determine the strength of
the Atlantic meridional overturning circulation (AMOC). This is defined as the maximum of the overturning stream function
below 1000m and north of 30°S, using only the flow field in the Atlantic Ocean.

We look at the temporal variability of SSTs through El Niño Southern Oscillation (ENSO), Atlantic/Pacific (Multi-)Decadal
200 Variability (AMV/PMV) and the AMOC time series. ENSO is characterised by the Niño indices, taking the monthly average
SST anomaly over 0–10 °S, 90–80°W (Niño 1+2) and 5°N–5°S, 170–120°W (Niño 3.4). To capture ENSO variability on
decadal time scales as well, we use 200 rather than 100 years of monthly SST data. We subtract the 12-monthly climatological
mean and apply a linear de-trending to each model grid point. The resulting Niño time series are then treated with a 5-month
running mean.

205 The calculation of AMV/PMV indices requires the use of empirical orthogonal functions (EOFs), using 500 years of annual
mean SST data as these processes occur on longer timescales (see e.g. Deser et al. 2012; Trenberth and Shea 2006, and
<https://climatedataguide.ucar.edu/data-type/climate-indices>; date of last access: 17/08/2021). We apply a local de-trending to
annual SST time series at each grid point by subtracting a 200-year smoothing spline. We then determine the first three spatial
EOFs of the resulting SST anomalies for the North Atlantic (10–70 °N) and North Pacific (20–60 °N) Ocean. The AMV mode
210 is then determined as the EOF of which the time series correlates best with the North Atlantic average SST, to not select a
mode that is dominated by e.g. ENSO or PMV. The PMV is simply the dominant EOF in the North Pacific Ocean, obtained
from the annual SST anomalies. Patterns of SST variability corresponding to these modes can then be obtained by correlating
the local SST anomalies to each of the specific mode time series.

We perform a spectral analysis of the different modes of variability, using a multi-tapered method (MTM) as it is more suitable



Table 1. Overview of globally averaged observables and equilibration measures for all of our simulated cases, including simulation length (+ denotes a continuation from the above control case), mean annual 2m air temperature (MAT), average tropical temperature MAT_T , average polar temperature MAT_P , mean annual precipitation (MAP), top of model net radiative flux (R_{TOM}), sea surface temperature (SST), full depth ocean temperature (OT), and ocean temperature drift. Subscript e denotes estimated equilibration values.

Measure Simulation	Length (years)	MAT (°C)	MAT_e (°C)	MAT_T (°C)	MAT_P (°C)	MAP (m yr ⁻¹)	R_{TOM} (W m ⁻²)	SST (°C)	OT (°C)	OT_e (°C)	OT Drift (10 ⁻⁴ K yr ⁻¹)
E²⁸⁰	3100	13.85	13.82	25.32	-22.51	1.046	-0.002	18.42	3.04	3.04	-1.03
E ^{280,P}	+2700	13.87	13.83	25.28	-22.30	1.044	+0.016	18.40	3.61	3.65	+1.56
E ⁵⁶⁰	+1000	16.54	16.75	27.25	-16.94	1.092	+0.187	20.23	4.14	5.14	+6.18
E ¹¹²⁰	+2000	19.86	20.16	29.52	-9.52	1.156	+0.214	22.66	6.66	8.15	+6.89
Eoi⁴⁰⁰	2000	18.54	18.47	28.02	-10.09	1.181	-0.073	21.89	7.28	7.09	-1.64
Eoi ²⁸⁰	+1000	17.17	16.78	27.01	-12.98	1.154	-0.139	20.86	6.53	6.25	-3.19
Eoi ⁵⁶⁰	+1500	19.91	19.88	29.01	-7.21	1.208	-0.042	22.97	8.28	8.27	+0.76

215 for climatic time series of limited length (Ghil et al., 2002). This method is based on a standard Fourier analysis, but uses
 tapers to limit cut-off effects at the edges of the respective time series. We apply this technique, using 3 tapers and a bandwidth
 parameter of 2. All of the resulting power spectra are tested against a red noise null hypothesis, using 10.000 random AR1
 surrogate time series. The median of these red noise power spectra is used to normalise those of the corresponding modes of
 variability, making the latter more easy to interpret as well as consider their statistical significance using 90%, 95%, and 99%
 220 confidence levels. Finally, we also correlate the time series of different modes: AMV, PMV, AMOC and ENSO (now using 500
 years of annual SST anomalies for the latter as well, rather than 200 years of monthly SST anomalies). These correlations are
 considered significant when their corresponding p-value is less than 0.05 (i.e. white noise null hypothesis).

4 Results

225 4.1 Global averages and climate sensitivity

An overview of globally averaged temperatures, drifts and radiative balance at the end of each of our model simulations is
 provided in Table 1. These values, including some additional metrics of the vertical thermal distribution of the ocean, are vi-
 sualised in Figure 3. Throughout the different cases, we see a consistent globally averaged equilibrium warming of $\sim 3^\circ\text{C}$ per
 CO_2 doubling in the near surface atmosphere. This warming response reduces slightly to $\sim 2.5^\circ\text{C}$ in the ocean. The globally
 230 averaged sea surface temperature (SST) only increases by $\sim 2.1^\circ\text{C}$ per CO_2 doubling, as a result of the inhomogeneous distri-
 bution of land/sea surface. There is some nonlinear response towards higher CO_2 concentrations, which is closely related to the



corresponding radiative forcing in the model. Starting from the pre-industrial reference, a single CO₂ doubling results in an initial perturbation of 3.49 W m⁻² while a quadrupling of CO₂ induces 7.93 W m⁻², meaning that the radiative forcing of 4×CO₂ is 2.27 (rather than 2) times that of 2×CO₂ (Baatsen et al., 2020). Using the corresponding deviation of the globally averaged near surface air temperature (2.93°C and 6.34°C in the E⁵⁶⁰ and E¹¹²⁰, respectively), we find a climate sensitivity parameter of 0.80–0.84 K W⁻¹ m². Using the E¹¹²⁰ extrapolated temperature, we report an estimated equilibrium climate sensitivity (ECS) of 3.17°C per CO₂ doubling, noting the nonlinearity towards higher pCO₂. Comparing the Eoi⁵⁶⁰-Eoi²⁸⁰ temperatures, we find a difference of 3.2°C, indicating a similar ECS between the modelled pre-industrial and Pliocene states. The observation that the Pliocene ECS tends towards the higher regime of pre-industrial (i.e. E¹¹²⁰-E⁵⁶⁰ rather than E⁵⁶⁰-E²⁸⁰) suggests that the nonlinearity in ECS is a function of the reference temperature rather than pCO₂, as the Eoi²⁸⁰ temperatures are comparable to the E⁵⁶⁰ ones.

Strikingly, the applied mid-Pliocene model boundary conditions result in an average warming similar to a doubling of atmospheric pCO₂ regardless of background CO₂ level. Looking at the upper (<1000m) versus deep (>2000m) ocean average temperatures in Figure 3, the offset between pre-industrial and mid-Pliocene conditions seems depth-dependent. While the upper ocean is about 2°C warmer in our mid-Pliocene simulations, the deep ocean is over 3.5°C warmer compared to the pre-industrial cases. Taking into account the extrapolated equilibrium temperatures of the E^{280,P} simulation as well, the vertical redistribution of heat can be attributed to the altered mixing parameters in the mid-Pliocene model set-up. After correcting the temperature offsets between pre-industrial and mid-Pliocene simulations, the global average again closely resembles that of a CO₂ doubling. A more detailed look into the distribution of different temperature responses to either external radiative forcing or model boundary conditions is presented in Section 4.5.

Compared to the E²⁸⁰ pre-industrial reference, the simulated climate of our Eoi⁴⁰⁰ mid-Pliocene control is on average almost 5°C warmer at the surface. This is accompanied by a 13% increase in mean annual precipitation and a considerable polar amplification factor. The latter is found by comparing the change in average polar (>66.5°N/S) to tropical (<23.5°N/S) temperature: MAT_P/MAT_T between different cases. This gives a polar amplification factor of 3.11 and 3.17 for the E⁵⁶⁰ and E¹¹²⁰, respectively, compared to the E²⁸⁰. A slightly smaller value of 2.85 is found between the Eoi⁵⁶⁰ and Eoi²⁸⁰, but a much larger polar amplification factor of 4.75 is seen between the Eoi⁴⁰⁰ and E²⁸⁰, including the effect of changing the model boundary conditions. This value increases further to 5.78 (Eoi²⁸⁰-E²⁸⁰) or 5.42 (Eoi⁵⁶⁰-E⁵⁶⁰) between Pliocene and pre-industrial cases at equal atmospheric pCO₂, indicating a strongly enhanced temperature response towards high latitudes to the applied Pliocene model boundary conditions.

As shown in Figure 3 and Table 1, the full depth average of the oceans is about 2.5°C warmer in our Pliocene simulations compared to the equivalent pre-industrial case at equilibrium. Differences in land ice cover and vegetation type, but also snow and sea ice coverage provide a substantial contribution to the modelled Pliocene warmth (see also Table S2 in the supplementary material). Shortwave surface fluxes alone account for a ~6 W m⁻² net forcing in the globally averaged radiative balance, comparing Pliocene to pre-industrial cases at equal pCO₂ (Eoi²⁸⁰-E²⁸⁰: 6.6 W m⁻²; Eoi⁵⁶⁰-E⁵⁶⁰: 5.4 W m⁻²). The responsible surface albedo feedback thus plays a primary role, decreasing slightly towards a warmer reference state. Although small, shortwave cloud feedbacks (Eoi²⁸⁰-E²⁸⁰: -1.2 W m⁻²; Eoi⁵⁶⁰-E⁵⁶⁰: 0 W m⁻²) counteract the reduced effect of surface albedo



270 towards warmer states, helping to explain why we see a similar climate sensitivity across all of our model cases. Longwave radiative fluxes play a similar role to enhance Pliocene warmth in our simulations, mainly through the lapse rate and water vapour feedback. A warmer ocean surface and atmosphere lead to an increase in the total column water vapour, which acts as a greenhouse gas. In contrast to shortwave fluxes, this effect becomes larger towards warmer conditions ($E_{oi}^{280} - E^{280}$: 11.4 W m^{-2} ; $E_{oi}^{560} - E^{560}$: 12.1 W m^{-2}), but is again mitigated by small longwave cloud feedbacks ($E_{oi}^{280} - E^{280}$: 0.7 W m^{-2} ; $E_{oi}^{560} - E^{560}$: 0.2 W m^{-2}).

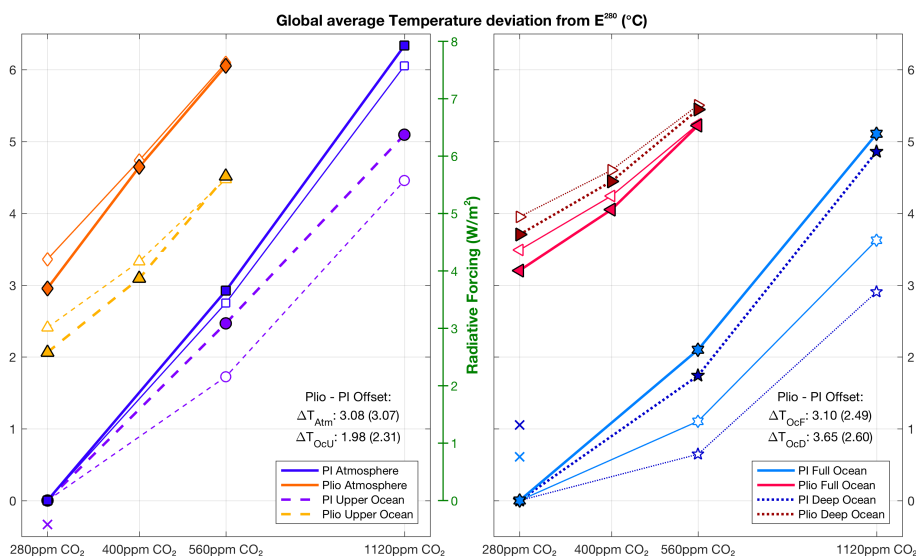


Figure 3. Overview of global average temperature in all of our different pre-industrial and Pliocene cases, compared to the E^{280} . Open markers, connected by thin lines, show the time mean at the of each simulation. Filled markers, connected by thick lines, show the corresponding equilibrium values. Cool colours are used for pre-industrial (*PI*) cases, warm colours for the Pliocene (*Plio*) ones. We consider 4 different temperature measures: near surface air temperature, upper ocean, full ocean, and deep ocean surface/volume weighted averages. Crosses indicate extrapolated temperatures from the $E^{280,P}$ case. Pliocene–pre-industrial offset values are given, determined by the mean temperature difference between cases at equal CO_2 (using a log interpolation between 280 and 560 ppm, to estimate the missing E^{400}). A similar offset, corrected for the difference between the E^{280} and $E^{280,P}$, is shown between brackets.

4.2 Simulated mid-Pliocene Conditions

4.2.1 Atmosphere

275 Looking at the annual mean near surface air temperature in the E_{oi}^{400} versus E^{280} case (Figure 4 a,b), we can identify the direct influence of many of the changes made in the PlioMIP2 mid-Pliocene boundary conditions. The strongest temperature deviations are seen over parts of Antarctica and Greenland in the absence of land ice. Relatively cool temperatures in the E_{oi}^{400} can be found over East Antarctica, where we have implemented a thicker ice sheet compared to the pre-industrial conditions.

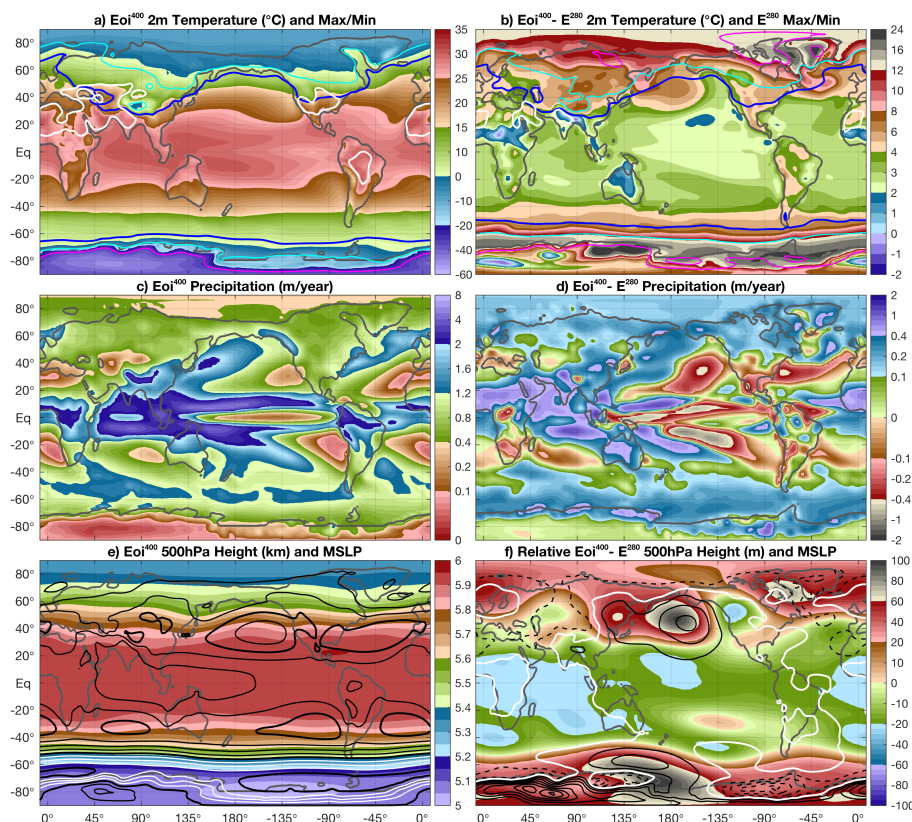


Figure 4. Annual mean atmospheric observables from our Eoi^{400} case (left) and the $Eoi^{400} - E^{280}$ difference. **a,b**) Near surface (2m) air temperature (shading), warmest month mean maximum (contours; white: 40°C), and coldest month mean minimum (contours; blue: 0°C, cyan: -10°C, magenta: -20°C). Contours in (a): Eoi^{400} ; in (b) E^{280} . **c,d**) Precipitation (m/year), differences in (d) are smoothed over land. **e**) Height of the 500hPa pressure level (shading) and mean sea level pressure (MSLP; contours every 5hPa, black ≤ 1000 hPa, white < 1000 hPa, thick line every 20hPa). **f**) 500hPa height difference with respect to the global average $Eoi^{400} - E^{280}$ value (i.e. 96m), contours are used for MSLP (every 2 hPa, solid > 0 , dashed < 0 , thick white line at 0hPa).

We see similar temperatures between the E^{280} and Eoi^{400} over much of the land at low latitudes, that are mainly a result of surface properties in the Pliocene boundary conditions that counteract the overall warming (e.g. lakes in Africa, vegetation in Australia, see also supplementary Figure 1). Warmest month mean temperatures of $> 40^\circ\text{C}$ occur over many low and middle latitude continental regions, while coldest month mean temperature contours steadily migrate poleward in the Eoi^{400} . As shown in Table 1, we see a considerable polar amplification in the overall warming pattern between the Eoi^{400} and E^{280} with mostly small temperature differences in the tropics increasing to $> 10^\circ\text{C}$ over both the Arctic and Southern Ocean.

Besides warmer, the Eoi^{400} is substantially wetter compared to the E^{280} (Figure 4 c,d) with a global average annual precipitation of 1180mm versus 1042mm (i.e. a 13%; see Table 1). Polar regions are overall wetter, but most noticeably over the Southern Ocean. This is in agreement with a larger ice volume over parts of East Antarctica. An overall poleward migration of storm



tracks is seen, which is most pronounced over the North Atlantic Ocean. At lower latitudes, changes in the precipitation pattern are dominated by a shift towards the Eastern Hemisphere. Regions surrounding the Indian and West Pacific Ocean are much wetter in the Eoi⁴⁰⁰ while those around the East Pacific and Atlantic Ocean become drier. This is related to a combined westward shift and expansion of the Walker circulation in our mid-Pliocene simulations. Like many other comparable model studies (see e.g. Bellucci et al. 2010; Haywood et al. 2020), our E²⁸⁰ shows a double inter-tropical convergence zone (ITCZ) over the Pacific Ocean. The southern branch of the ITCZ is weaker over the Pacific Ocean in the Eoi⁴⁰⁰, while shifting westward and southward towards a pronounced South-Pacific Convergence Zone (SPCZ). A more active Indian Monsoon can explain increased rainfall over the Middle East and South Asia, as well as some of the cooler temperatures in northern India. Higher precipitation rates in the Eoi⁴⁰⁰ are also seen over Australia and much of northern Africa, which are directly related to the altered land surface properties (see also Figure S1 in the supplementary material).

In addition to the direct effects of the PliomIP2 boundary conditions, some more general changes in the atmospheric circulation are seen between the E²⁸⁰ and Eoi⁴⁰⁰ cases (Figure 4 e,f - note that the global average change in 500hPa height is subtracted in f). A reduction in the equator-to-pole gradient is not only present in surface temperatures, but also in mid-tropospheric height surfaces. This translates to an overall reduction of baroclinic instability, despite some of the increases in precipitation seen at middle and high latitudes. Reduced surface elevation over much of West Antarctica and Greenland leads to a lower surface pressure in the Eoi⁴⁰⁰ while the opposite is seen over parts of East Antarctica. These changes in the surface topography also likely influence the circulation as several stationary ridges are evident in the 500hPa height difference. Preferred midlatitude ridging is evident over the North Pacific Ocean in the Eoi⁴⁰⁰, which is in turn reflected in the temperature and precipitation differences with the E²⁸⁰.

4.2.2 Ocean

Annual mean sea surface temperatures (SSTs) reflect the patterns and changes seen in the Eoi⁴⁰⁰ and E²⁸⁰ atmospheric temperatures (Figure 5 a,b; a similar comparison using the E^{280,P} instead can be found in supplementary Figure 8). In contrast to near surface air temperature, the Arctic Ocean SSTs show the smallest difference between the Eoi⁴⁰⁰ and E²⁸⁰ cases despite large reductions in sea ice cover. Another area with relatively cool temperatures in the Pliocene is the eastern Tropical Pacific Ocean, being still ~2°C warmer compared to the E²⁸⁰. Much warmer SSTs are seen over much of the North Atlantic Ocean, as well as the Northwest Pacific Ocean. Apart from the West Antarctic coastal region, the entire Southern Ocean is ~4–8 °C warmer in our Pliocene control.

Sea surface salinity (SSS) patterns in the Eoi⁴⁰⁰ are mostly driven by precipitation patterns and gateway changes (Figure, 5c,d) between the E²⁸⁰. High precipitation amounts over most of Asia and the Indian Ocean cause low SSS through surface fluxes as well as river runoff. The Arctic Ocean is less saline compared to the E²⁸⁰ partly as a result of increased runoff, but also due to the closed Bering Strait and Northwest Passage. The outflow of these low salinity Arctic surface waters can be seen to the east and south of Greenland, resulting in a rather complex interaction with much more saline waters in the northern Atlantic Ocean. The Pacific Ocean is in general more saline in the Eoi⁴⁰⁰, with regional changes from the E²⁸⁰ that are the combined effect of precipitation patterns, enhanced river runoff, and the Bering Strait closure.

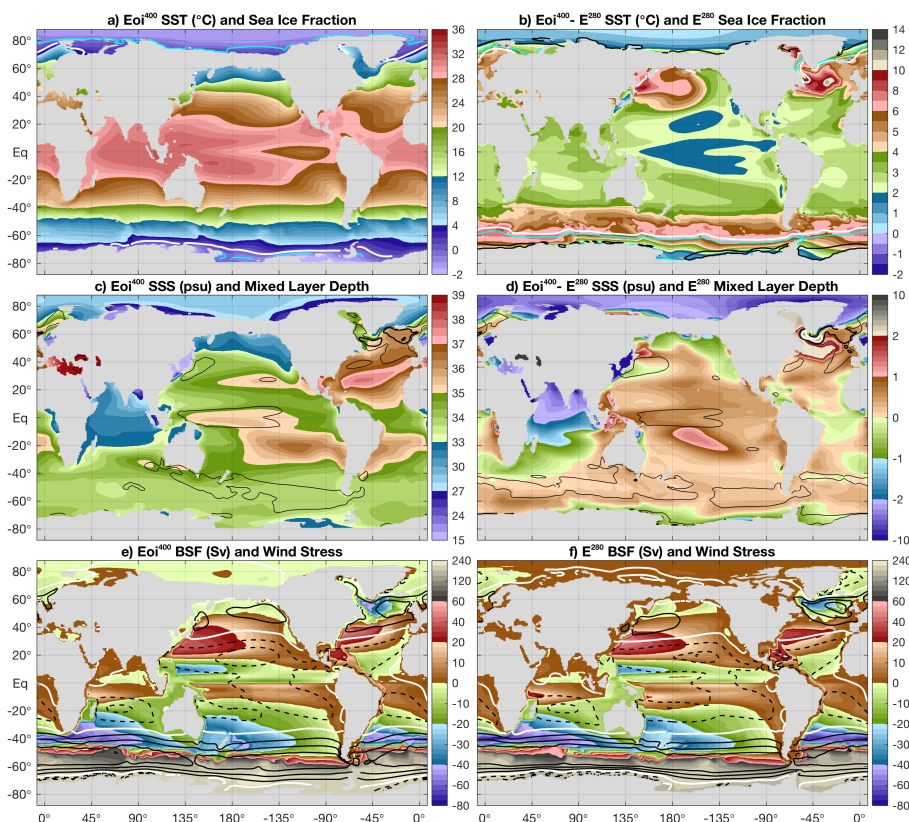


Figure 5. Annual mean oceanic observables from our Eoi^{400} case (left) and the $Eoi^{400}-E^{280}$ difference. **a,b** sea surface temperature temperature (shading) and sea ice fraction (contours; white: 0.15, cyan: 0.5, black: 0.9). Contours in (a): Eoi^{400} ; in (b) E^{280} . **c,d** Sea surface salinity (shading) and mixed layer depth (thin line: 100m, thick black: 250m, thick white: 500m). **e,f** Barotropic stream function (BSF; shading) and zonal wind stress (contours every $5 \cdot 10^{-2} Pa$, dashed: <0 , thick white line at $0 Pa$). Contours in (e): Eoi^{400} ; in (f) E^{280} .

The depth averaged flow, represented by the barotropic stream function (BSF) in Figure 5 e,f is very similar between the Eoi^{400} and E^{280} cases. Regardless of the reduced meridional gradient in surface temperatures, the Antarctic Circumpolar Current (ACC) is slightly stronger in our Pliocene control. In contrast to what is seen at the surface, the depth-averaged density gradient is steeper in the Eoi^{400} and therefore enhances the density-driven component of the ACC. Southern Hemisphere subtropical gyres are slightly weaker, while those in the Northern Hemisphere show a poleward extension in the Eoi^{400} . North Atlantic subtropical and subpolar gyres are both stronger compared to the E^{280} .

4.2.3 Sea ice

Even with the relatively simple model set-up used here, our E^{280} simulation has realistic sea ice cover compared to late 20th century observations from Peng et al. (2013) as shown in Figure 6. The mean sea ice maximum extent corresponds well with the observed modern day maximum in both hemispheres, but the minimum is overestimated especially in the Southern Hemisphere.

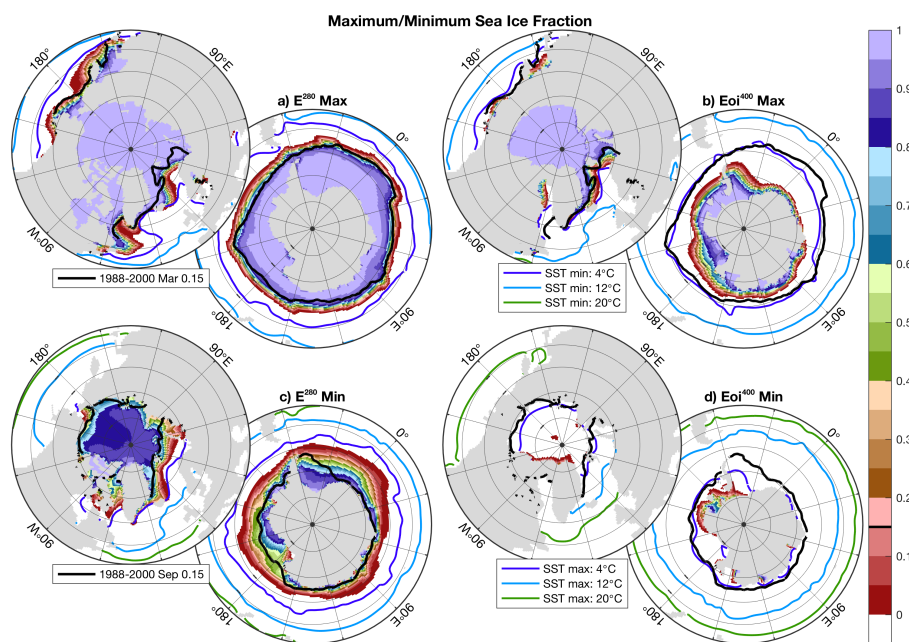


Figure 6. **a)** E^{280} mean maximum monthly sea ice fraction over northern and southern polar regions. Coloured contours show coldest month mean SST, black contour indicates the late 21st century observed September (NH)/March (SH) sea ice edge at an 0.15 fraction (Fetterer et al., 2017). **b)** As in (a), but for the Eoi^{400} case using the same contour intervals and sea ice edge data. **c-d)** Similar to (a-b) showing the monthly sea ice minimum, warmest month mean SST and late 21st century observed March (NH)/September (SH) sea ice edge.

The disagreement may, however, be mostly explained by the difference between pre-industrial and modern conditions. Sea ice cover is drastically reduced in our Eoi^{400} simulation compared to the E^{280} one. During the late summer minimum extent, sea ice concentrations drop to nearly zero across both polar regions, with only some remaining over exposed waters in West Antarctica. Changes in the maximum sea ice cover are less dramatic over the Arctic region, while the Southern Ocean still has much less sea ice cover in the Eoi^{400} compared to the E^{280} case. This corresponds well with the $\sim 4\text{--}8^\circ\text{C}$ warmer SSTs seen across the Southern Ocean in our Pliocene simulations (Figure 5b). The isolated nature of the Arctic Ocean allows its surface waters to remain relatively cool, with some sea ice persisting until late summer. Despite substantial refreezing during wintertime, open waters in the early winter months prevent the air from cooling down further. This explains the much larger near surface air temperature anomalies over the Arctic region between our Eoi^{400} and E^{280} simulations (Figure 4b).

4.3 Meridional overturning and heat transport

4.3.1 Global

Our Eoi^{400} case is characterised by a stronger and deeper global meridional overturning circulation (MOC) compared to the E^{280} . This is reflected in the global meridional overturning stream function (MSF) in Figure 7a,b by the dominant northern

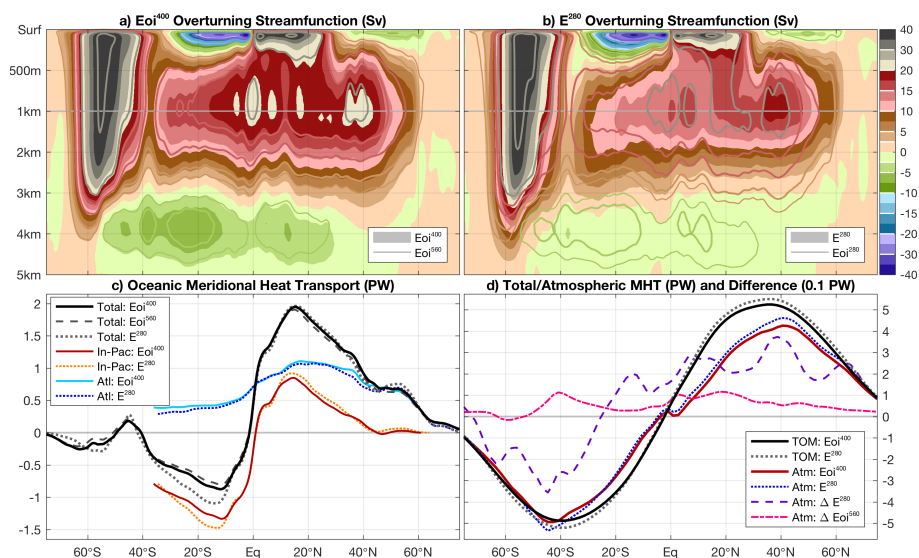


Figure 7. **a)** Global oceanic meridional overturning stream function (MSF) of the Eoi⁴⁰⁰ (shading) and Eoi⁵⁶⁰ (contours) simulations, taking the mean over the last 100 model years. **b)** As in (a), but for the E²⁸⁰ and Eoi²⁸⁰ cases. Note the vertical stretching of the upper 1km, used contour intervals are highlighted in white on the colour bar. **c)** Oceanic meridional heat transport in the Eoi⁴⁰⁰ (solid lines; global: black, Indo-Pacific: red, and Atlantic Ocean: blue), E²⁸⁰ (dashed lines, similar colouring), and Eoi⁵⁶⁰ (dotted line, only global). **d)** Total meridional heat transport, induced by the top of model (TOM) net radiative fluxes (black) and the corresponding atmospheric heat transport (red) in the Eoi⁴⁰⁰. Similar for the E²⁸⁰ using grey and blue dotted lines, respectively. The difference (Δ) in atmospheric heat transport with respect to the Eoi⁴⁰⁰ is shown for the E²⁸⁰ (dashed pink) and Eoi⁵⁶⁰ (dash-dotted pink), magnified tenfold.

345 overturning cell north of 40°S. The deep southern (i.e. negative) overturning cell linked to Antarctic bottom waters is slightly stronger in the Eoi⁴⁰⁰ as well. Note that the appearance of this overturning cell is mostly masked in the Southern Ocean by strong Ekman upwelling linked to the ACC. The Eoi⁵⁶⁰ MOC is similar to the Eoi⁴⁰⁰ one, but overall slightly weaker, while the opposite holds for the Eoi²⁸⁰. This can be partly a transient effect of the simulations, but suggests a tendency of the MOC to get weaker towards higher atmospheric pCO₂.

350 The differences in MSF pattern and strength between the Eoi⁴⁰⁰ and E²⁸⁰ cases are only partly reflected in the corresponding oceanic heat transports (OHT), shown in Figure 7c. Apart from a slight weakening of poleward heat transport at southern low latitudes (mostly in the Indo-Pacific sector), the Eoi⁴⁰⁰ OHT is very similar to the E²⁸⁰. The warmer Eoi⁵⁶⁰ case has an overall reduced poleward oceanic heat transport, but the relative change is small (<0.1PW). The total meridional heat transport (MHT, shown in Figure 7d), is slightly weaker in the Eoi⁴⁰⁰ compared to the E²⁸⁰. This is a direct response the reduced meridional temperature gradient seen in the Eoi⁴⁰⁰, demanding a lower poleward heat transport on both hemispheres. As there are only minor changes in the oceanic component, the reduced total MHT must be mainly accounted for by the atmosphere. This is clearly reflected atmospheric MHT difference of E²⁸⁰ with respect to the Eoi⁴⁰⁰, having mostly the same sign as the total MHT. The only exception is seen at southern low latitudes, where a stronger southward OHT is compensated by a northward

355



360 atmospheric MHT in the E^{280} . The E^{560} atmospheric MHT shows a small net positive offset with respect to the E^{400} , that may be explained by some remnant warming trend. In agreement with a further reduction of the meridional temperature gradient, the warmer E^{560} case thus has a further reduced poleward MHT albeit small ($\sim 0.1 \text{ W m}^{-2}$) and mostly accounted for by the ocean.

4.3.2 Atlantic Ocean

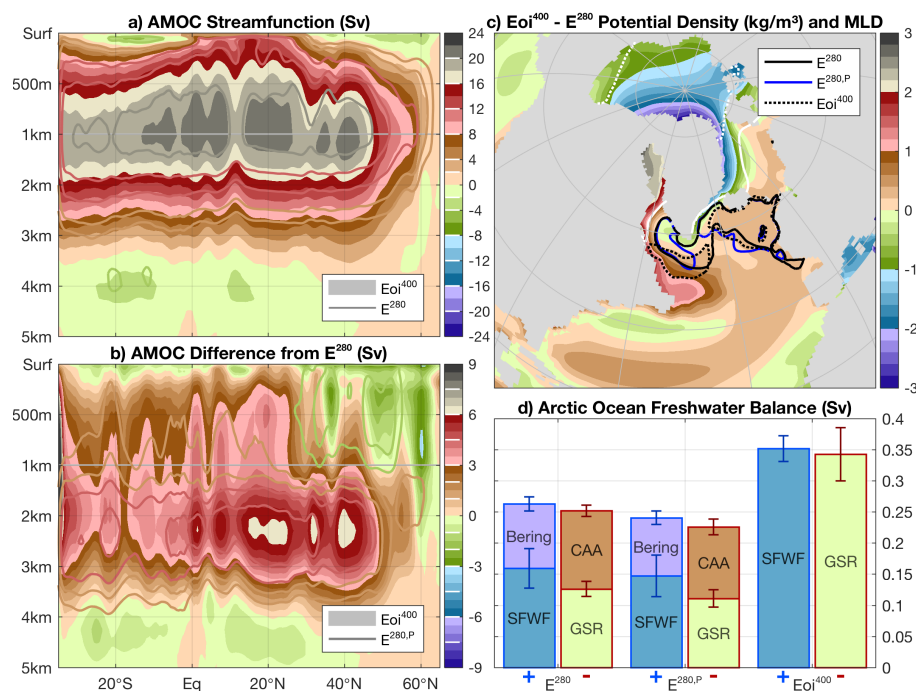


Figure 8. **a)** Mean AMOC stream function over the last 500 years of the E^{400} (shading) and E^{280} simulation (contours, highlighted on the colour bar). **b)** Difference in AMOC stream function with respect to the E^{280} , for the E^{400} (shading) and the $E^{280,P}$ (contours). **c)** $E^{400} - E^{280}$ (100-year mean) potential density difference, averaged over the upper 100m and relative to the global average change. Contours show the annual mean maximum mixed layer depth for the E^{280} (solid black), $E^{280,P}$ (solid blue), and E^{400} (dotted black). **d)** Freshwater budget over the Arctic Ocean for the (left to right) E^{280} , $E^{280,P}$, and E^{400} cases, including the net surface freshwater flux (SFWF) and transports across the Bering Strait, Canadian Archipelago (CAA), and Greenland-Scotland Ridge (GSR). The mean over the last 500 model years is taken, with the standard deviation of yearly averages indicated by the error bars.

365 The Atlantic Meridional Overturning Circulation (AMOC; Figure 8a) clearly encompasses the entire deep northern over-turning cell in the global MSF north of 30°S (Figure 7a). The AMOC mean state is overall stronger in our Pliocene versus pre-industrial simulations, but its temporal variability is also considerably higher in all of the Pliocene cases ($22.7 \pm 1.6 \text{ Sv}$ versus $18.3 \pm 0.7 \text{ Sv}$; see also Figure S5 in the supplementary material). Especially the E^{560} AMOC undergoes a series of large ($>10\text{Sv}$) intensity swings, although this is likely caused by the thermal adjustment of the deep ocean and therefore



mostly a transient model feature. These large swings stopped after ~ 1000 model years, but the AMOC variability remains
370 the largest of any of our cases ($\sigma = 2.4\text{Sv}$). The $E^{280,P}$ AMOC also exhibits a larger variability ($\sigma = 1.0\text{Sv}$) compared to the
other pre-industrial cases, but still smaller than any of the Pliocene ones. A more detailed discussion on AMOC variability is
provided in Section 4.6.2

The difference in AMOC streamfunction between Eoi^{400} and E^{280} is most pronounced between 1 and 3 km depth (Figure
8b). The stronger and deeper AMOC cell can be partly explained by the altered vertical mixing parameters in our Pliocene
375 model set-up, as the $E^{280,P}$ shows a reduced but very similar difference pattern with respect to the Eoi^{400} . In general, we find
that the altered vertical mixing scheme in our Pliocene simulations does have an impact on the strength and behaviour of the
AMOC, but not to the extent that is seen in any of the Pliocene cases. It is therefore likely that the altered boundary conditions
and resulting circulation changes have a considerable impact on the AMOC strength and behaviour. The applied PlioMIP2
boundary conditions include the closure of several high latitude oceanic gateways. This results in lighter upper ocean waters
380 across the Arctic Ocean in the Eoi^{400} , but denser waters across most of the North Atlantic Ocean (Figure 8c). The integrated
net surface freshwater flux over the Arctic Ocean more than doubles in the Eoi^{400} case compared to the E^{280} one (Figure 8d).
This more than compensates for the missing transport from the Bering straight closure. Lacking connectivity through the Cana-
dian Archipelago demands for an equally large net southward freshwater transport across the Greenland-Scotland ridge. The
outflow of those light, low salinity Arctic waters pushes the deep water formation zone towards the south across the Labrador
385 Sea into warmer and deeper waters. Increased salinity in the Labrador Sea and thus higher potential densities are tied to the
closure of the Canadian Archipelago, as shown by the negative component in the E^{280} Arctic Ocean freshwater balance (i.e.
net salt transport from Labrador Sea). Such a southward shift of the deep water formation zone is not present in the $E^{280,P}$ case.

4.4 Model-proxy comparison

As shown by Haywood et al. (2020), our Eoi^{400} case performs well when comparing the annual mean SSTs to the available
390 PlioMIP2 time-specific proxy records (Foley and Dowsett, 2019). The zonally averaged, annual mean SST from our different
simulations is shown in light of these proxies in Figure 9a. Considering site-specific rather than zonally averaged SSTs from the
 Eoi^{400} simulations, we find a root mean square error (RMSE) of 3.5°C and a mean absolute error (MAE) of 2.5°C . Moreover,
there is no significant warm or cold model bias across the SST/latitude range covered by the proxies. Relatively warm North
Atlantic SSTs in the model are well reflected by the proxy record, apart from a single site in the high latitude North Atlantic
395 (ODP site 909) where our Eoi^{400} case is showing a $\sim 15^\circ\text{C}$ lower SST.

Looking at the SST difference between Pliocene and pre-industrial conditions, rather than absolute values, reveals some more
discrepancies between proxy records and our Eoi^{400} simulation (Figure 9b). Most of the high positive temperature anomalies at
northern middle and high latitudes remain well captured by the model, as well as the much smaller differences at low latitudes.
However, other sites at both northern and southern middle latitudes show a much poorer agreement between model-based and
400 proxy indicated Pliocene - pre-industrial SST differences. The lack of proxy data across most of the Southern Ocean makes
it impossible to assess whether the large SST differences between our Pliocene and pre-industrial simulations are realistic.
Despite the seemingly poor visual agreement compared to absolute Pliocene SSTs, RMSE and MAE indices are only slightly

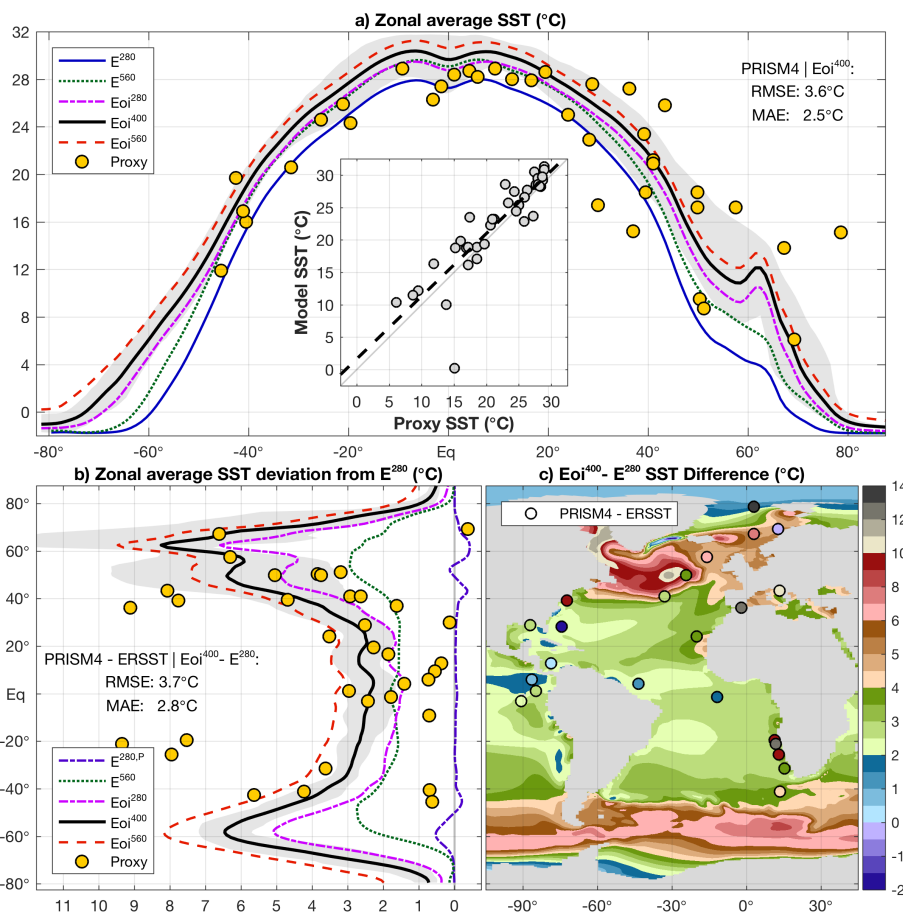


Figure 9. a) PRISM4 proxy-based annual mean SST reconstructions (yellow markers) versus model-derived zonally averaged SST for Eoi^{400} (black, including zonal variation in grey), E^{280} (blue), E^{560} (green dotted), Eoi^{280} (pink dash-dotted), and Eoi^{560} (orange dashed). The inset shows a point-wise comparison, including a simple linear regression. b) Pliocene proxy - pre-industrial SST (ERSST; late 19th century reanalysis) and modelled zonal average SST difference from E^{280} (colouring as in a; purple dash-dotted: $E^{280,P}$). c) Pliocene - pre-industrial SST difference over the Atlantic Ocean: proxy - PI reanalysis (coloured markers) and model-derived $Eoi^{400} - E^{280}$ (shading).

lower for the Pliocene - pre-industrial difference.

Surprisingly large Pliocene - pre-industrial SST differences (considering a limited CO_2 effect) were found in the PliMIP1, especially over the North Atlantic Ocean, but not well reflected in the model ensemble (Haywood et al., 2013b). This seems to be greatly improved now, as shown by the large positive anomalies over much of the middle to high latitude North Atlantic Ocean in Figure 9c. The largest discrepancies between proxy-based and model-derived Pliocene - pre-industrial SST differences are seen in the Mediterranean Sea and off the coasts of northern America and southern Africa. These discrepancies can be largely explained by coastal upwelling and boundary currents, which are poorly resolved in our simulations because of the limited horizontal resolution (e.g. McClymont et al. 2020). Although absolute Pliocene SSTs seem to agree better, they are



already much too warm at some of these locations in our E^{280} case compared to reanalysis data.
Near surface air temperatures reveal the same warming pattern between the Eoi^{400} and E^{280} case as seen in the SSTs over low and middle latitudes (see also Figure S9 in the supplementary material). The highest temperature anomalies shift poleward, over the Arctic Ocean and the Antarctic coastal region due to sea ice melt and reduced ice sheet cover. It is noteworthy that
415 even our coolest Pliocene simulation (Eoi^{280}) is similar or even warmer than the E^{560} case at all latitudes. This indicates the importance of the implemented mid-Pliocene model boundary conditions and long-term impacts such as the partial loss of ice sheets.

4.5 Sensitivity to Pliocene boundary conditions versus atmospheric pCO_2

Using our set of pre-industrial and Pliocene *sensitivity* simulations (i.e. E^{280} , E^{560} , Eoi^{280} , and Eoi^{560}), we can make an assess-
420 ment of the effects of the applied Pliocene boundary conditions (Eoi^n - E^n) versus external radiative forcing (X^{560} - X^{280}), as well as any state-dependency in the model response. The difference in annual mean near surface air temperature is shown in Figure 10. The top panels of this figure show the modelled temperature response to a shift from pre-industrial to Pliocene boundary conditions (excluding CO_2), the bottom ones to a doubling atmospheric pCO_2 . Consequently, comparing left to right panels shows the state-dependency of the effect of boundary conditions to a different pCO_2 baseline (top), and vice versa (bottom).
425 Some generic temperature differences between the model cases can be easily identified in all of these comparisons. Stronger contrasts are seen over land than over the ocean, as a result of the thermal capacity and much larger potential for latent heat fluxes over the ocean. Polar amplification of the temperature change also seems universal across our simulations, caused mainly by ice-albedo feedbacks and reversed lapse rate feedbacks (i.e. positive at high latitudes, negative at low latitudes). As noted before, the ECS of our simulated Pliocene climate is very similar to that of the pre-industrial one (i.e. $3.2^\circ C$ versus $3.17^\circ C$ per
430 CO_2 doubling). It is therefore not surprising that the overall response to a doubling of atmospheric pCO_2 is comparable, with mainly some regional differences as a result of the boundary conditions and local feedback mechanisms.

A similar comparison of atmospheric temperatures between our four *sensitivity* cases is made in Figure S7 in the supplementary material, showing the zonally averaged vertical distribution. The combination of surface albedo and lapse rates causes low latitude regions to warm mostly in the upper troposphere, while high latitude regions do so near the surface. This general response
435 is again seen in all of the four comparisons made between the *sensitivity* cases, with the exception of stronger high latitude warming near the surface after introducing Pliocene boundary conditions and stratospheric cooling in response to higher pCO_2 . We also observe a more negative lapse rate feedback in the warmer Pliocene cases, mostly at low and middle latitudes, likely as a result of higher SSTs and atmospheric moisture.

Most of the effects of the Pliocene model boundary conditions on temperature (Figure 10 a,b) agree well with those seen
440 earlier between our E^{280} and Eoi^{400} cases, shown in Figure 4b. The warming effect of removing/lowering ice sheets at high latitudes and cooling effect of introducing lakes or removing desert at low latitudes are independent of the atmospheric CO_2 level. Over the Arctic Ocean, reduced sea ice in the Pliocene simulations has an increased impact on temperatures above the surface towards lower pCO_2 (Figure 10 a vs. b). The opposite is seen over parts of the Southern Ocean, where sea ice cover is still relatively large in the E^{560} (see also contours in Figure 11). Temperature changes that can be related to altered circula-

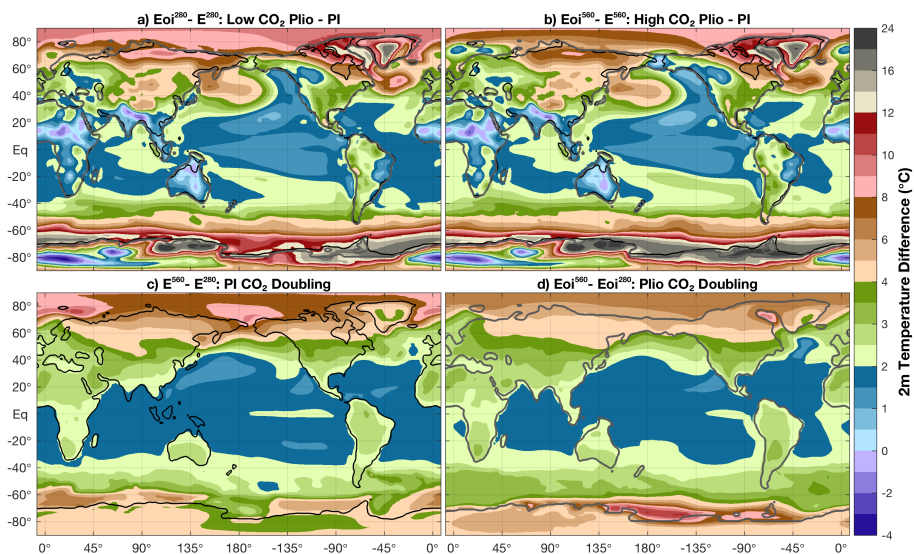


Figure 10. Annual mean near surface air temperature difference between our four *sensitivity* simulations; **a)** $Eoi^{280} - E^{280}$, **b)** $Eoi^{560} - E^{560}$, **c)** $E^{560} - E^{280}$, and **d)** $Eoi^{560} - Eoi^{280}$.

445 tion patterns in the Pliocene versus pre-industrial (e.g. monsoons, South Pacific Convergence Zone, midlatitude ridging, storm tracks) are robust between different CO_2 levels.

The temperature response to a doubling of atmospheric pCO_2 is very similar at low and middle latitudes between our pre-industrial and Pliocene simulations (Figure 10 c,d). Differences in sea ice cover (and to a lesser extent land ice and surface properties) amplify high latitude warming in response to a CO_2 doubling, most prominently over the Arctic in the pre-industrial 450 cases and over the Southern Ocean in the Pliocene ones.

The near surface air temperature differences between our four *sensitivity* cases (Figure 10) are reflected in the SST, as shown in Figure 11. The most prominent exception to this consistency is found over high latitude surface waters, which are seen to change much less in temperature than the air above. Moreover, any comparison showing a relatively large difference in near surface air temperature has a reduced SST difference over the same high latitude waters (e.g. Figures 10 and 11; a,c vs. b,d for the Arctic Ocean). This can be explained by the decoupling effect of sea ice, which tends to dampen the SST differences. Contour lines in Figure 11 indeed suggest a large reduction in sea ice cover over the Southern Ocean for $Eoi^{560} - Eoi^{280}$, while little change is seen for $E^{560} - E^{280}$. Also over the Arctic Ocean, the dampening effect of sea ice on SST differences is stronger for cooler reference states (Figure 11 a,c vs. b,d). The annual mean sea ice edge at northern high latitudes shows limited changes 460 between the simulations, as the effect is highly seasonal (strong reductions in summer, see also Figure 6).

The SST difference over the Pacific Ocean between Pliocene and pre-industrial cases is consistent between CO_2 levels and noticeably different from the effect of a pCO_2 doubling. These patterns suggest a shift in the background state of both ENSO and PDO in our Pliocene simulations (see also Section 4.6). An even more prominent and consistent SST response to the

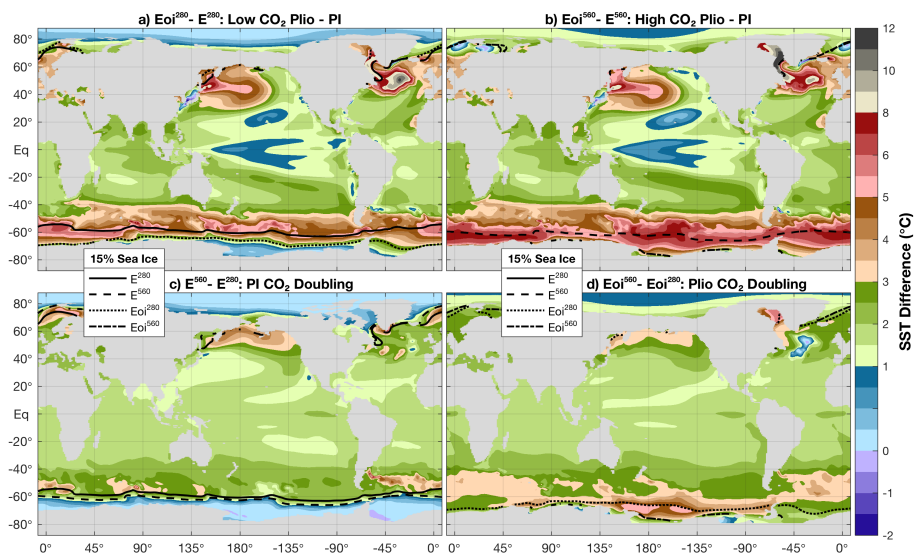


Figure 11. As in figure 10, but for sea surface temperature (SST), showing also the annual mean sea ice edge (i.e. 0.15 ice fraction) in black contours; solid: E^{280} , dashed: E^{560} , dotted: Eoi^{280} , and dash-dotted: Eoi^{560} (only 2 shown per panel).

Pliocene boundary conditions is found over the North Atlantic Ocean. This is likely the combined result of a stronger Pliocene AMOC and the isolation of the Labrador Sea through closure of the Canadian Archipelago. Large changes in SST between our Pliocene and pre-industrial simulations are also seen in the Southern Ocean. These can be linked to the upwelling of relatively warm deep waters south of the ACC. In contrast to the dampening effect of sea ice, the effect of upwelling near the ACC is the same at or above the ocean surface.

470 4.6 Modes of internal variability

4.6.1 El Niño Southern Oscillation

Not only the mean state, but several modes of variability in our simulated Pliocene climate are also different from what is seen in the pre-industrial reference. As it plays a primary role in the tropics, we first look at the behaviour of the El Niño Southern Oscillation (ENSO). In Figure 12, time series of the Niño 1+2 and Niño 3.4 indices are shown for the E^{280} and Eoi^{400} case. The amplitude of both ENSO indices is greatly reduced in our Eoi^{400} versus E^{280} case (σ_{1+2} : -54%; $\sigma_{3.4}$: -68%). This is the largest such reduction seen among the PlioMIP2 ensemble, as shown by Oldeman et al. (2021). Furthermore, the occurrence of strong and long-lasting ($>1^\circ\text{C}$; >1 year) El Niño/La Niña events completely disappears in our mid-Pliocene simulation. Both these findings are consistent among all of our mid-Pliocene (i.e. Eoi^{280} , Eoi^{400} , Eoi^{560}) versus pre-industrial (i.e. E^{280} , $E^{280,P}$, E^{560} , E^{1120}) cases (not shown).

480 Spectral analysis of the Niño 3.4 indices also shows large differences between the ENSO behaviour in the E^{280} and Eoi^{400}

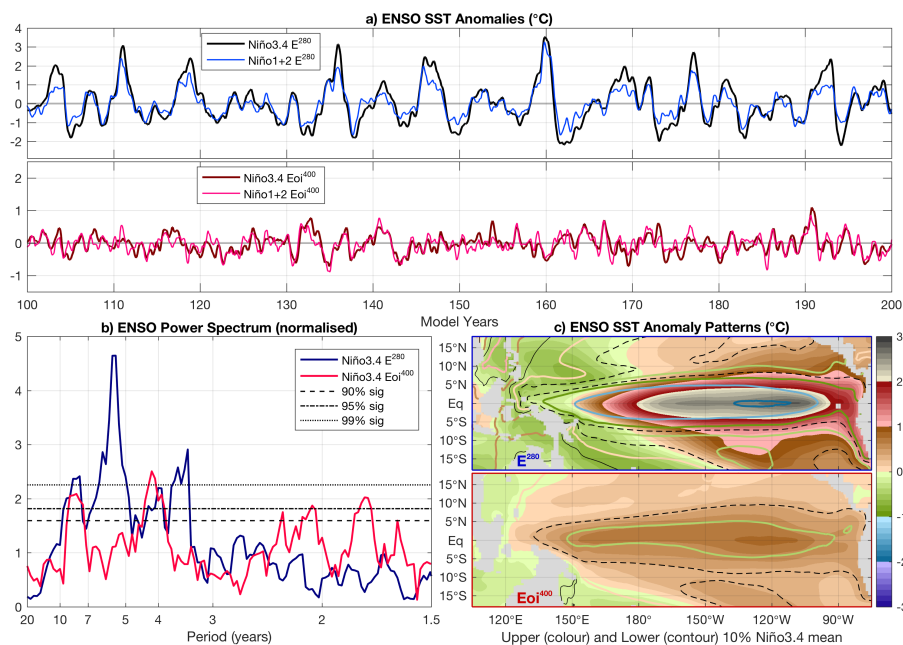


Figure 12. **a)** ENSO time series for the E^{280} (blue) and Eoi^{400} (red), using monthly SST anomaly fields and a 5-month running mean. Note the different scaling; temperature intervals are kept the same for visual comparison. **b)** Multi-taper power spectrum, using 200 years of monthly data including 90%, 95% and 99% confidence levels based. **c)** Corresponding ENSO SST patterns, taking the mean over the 10% highest (shading) and 10% lowest (contours) monthly Niño 3.4 index values at each location.

case. The modelled pre-industrial ENSO variability is characterised by a broad spectral peak at periods of 3–10 years, with 3 statistically significant (at 99% confidence) peaks and a dominant period around 6 years. A similar broad peak is seen for the mid-Pliocene ENSO, but only with significant variability at 4 years (99%) and 9 years (95%). Moreover, there is a lot more significant variability in the Eoi^{400} case at shorter periods around 2 years or less. This agrees well with the predominantly weak and rather high frequent behaviour of the modelled Pliocene ENSO, seen in the Niño 3.4 time series.

As to be expected from both of the Niño time series shown for each case, the amplitude of SST anomalies is seen to be much smaller throughout the tropical Pacific Ocean in our Eoi^{400} versus E^{280} case. Looking at the mean SST pattern corresponding to the 10% average highest and lowest monthly Niño 3.4 values allows us to assess both the spatial distribution and strength of ENSO variability at the same time. In addition to an overall highly reduced amplitude, the associated region of SST variability expands westward and poleward across the Central/West Pacific Ocean in our Pliocene simulation. The mean difference in SST between the Eoi^{400} and E^{280} (Figure 5b) over the main region of ENSO variability is smaller than the average tropics. The background state of the tropical Pacific Ocean is therefore not El Niño-, but rather slightly La Niña-like (see also Oldeman et al. 2021).

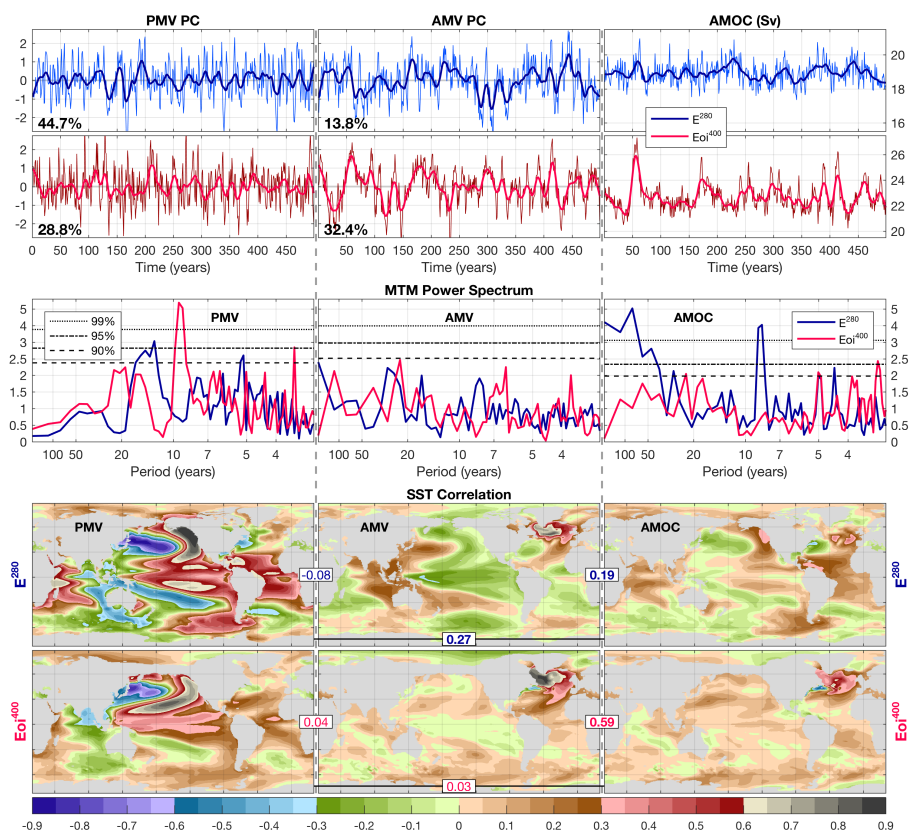


Figure 13. Time series (upper panels; thick lines using a 20-year smoothing window), multi-tapered power spectra (middle panels), and spatial correlation patterns (lower panels) of North Pacific SST (left), North Atlantic SST (middle), and AMOC strength (right) variability, for 500 years of annual SST data from our E²⁸⁰ (blue) and Eoi⁴⁰⁰ (red) simulation. The percentage of variance explained by the respective principal component is shown in black along with the PMV and AMV time series. Spatial SST patterns show the temporal correlation between the SST at each location and the different variability indices. Boxed numbers also indicate the total correlation between each of these indices (i.e. time series in the upper panels.)

4.6.2 Interannual to multi-decadal SST variability

495 Using 500 years of annual mean SSTs and AMOC strength, we assess the dominant modes of variability in the North Pacific and North Atlantic Ocean (Figure 13). We consider the dominant eigenmode of SST anomalies in the North Pacific Ocean to represent the PMV, and the one best correlating with average North Atlantic SSTs as the AMV. The explained variance by the PMV mode is seen to decrease in the Eoi⁴⁰⁰ versus E²⁸⁰ case, while that of the AMV greatly increases. As noted earlier, the AMOC variability is considerably larger in the Eoi⁴⁰⁰ case compared to the E²⁸⁰ one. Correlations between the PMV, AMV, AMOC and annual Niño 3.4 indices can be found in Figure S10 in the supplementary material.

500 Spectral analysis shows that the E²⁸⁰ PMV has a broad peak at 10–20 years and therefore strongly resembles the Pacific Decadal



Oscillation (PDO). This broad peak is seen to shift towards longer periods for the Eoi^{400} PMV, which is now accompanied by a sharper peak at just under 10 years. Looking at the patterns of SST variability associated to the PMV, an almost global footprint in the E^{280} is reduced to mostly a North Pacific signature in the Eoi^{400} . This is likely related to the strongly decreased ENSO variability in the Eoi^{400} versus E^{280} case, as both the low latitude SST patterns and the spectral properties at periods <10 years show a high resemblance between PMV and ENSO in both simulations. This is supported by significant correlations (E^{280} : 0.48; Eoi^{400} : 0.34) between the PMV and yearly Niño 3.4 indices. The role of the AMV on global SST variability is much more limited compared to PMV, but again strongest and more widespread in the E^{280} case. Meanwhile, the Eoi^{400} has a much higher percentage of explained variance and is strongly connected to AMOC variability. The spatial pattern of SST anomalies associated to the AMOC strength shows little resemblance to either the PMV or AMV in the E^{280} case, but both their time series are significantly (yet weakly) correlated. In contrast, the AMOC strength strongly correlates with the AMV for the Eoi^{400} and their associated spatial patterns show a large resemblance. It is thus clear that the stronger and more variable AMOC in our Pliocene simulations has a profound impact on not only the mean North Atlantic SSTs, but also their variability. Additionally, it seems that the different modes of SST variability are less connected between ocean basins in the Eoi^{400} versus E^{280} case.

515 5 Conclusions

We have completed a set of simulations using the CCSM4/CESM1.0.5 within the PlioMIP2, including E^{280} , E^{560} , Eoi^{280} , Eoi^{400} , and Eoi^{560} cases ($E^{280,P}$ and E^{1120} as additional sensitivity experiments). Our simulations show a warm mPWP climate, which is 4.7°C warmer compared to our pre-industrial control in terms of globally averaged near surface air temperature. With an estimated ECS of 3.1°C per CO_2 doubling, which is consistent throughout the different pre-industrial and Pliocene cases, much of the mPWP signal is thus related to the effect of the applied PRISM4 boundary conditions. The effect of those boundary conditions is mainly to increase temperatures by about 3°C on average globally and 2.4°C in the ocean. The vertical distribution of oceanic temperatures is altered in our Pliocene simulations by the use of enhanced background vertical diffusivity. The additional $E^{280,P}$ experiment shows that this differential warming patterns can be fully explained by the effect of this different parameter choice between the pre-industrial and Pliocene experiments. None of the other results are significantly influenced by the altered vertical diffusivity, with only minor regional differences seen at the surface and throughout the atmosphere.

The combined effect of increased atmospheric $p\text{CO}_2$ and altered boundary conditions not only make our Eoi^{400} case warmer than the E^{280} one, but also induce substantial polar amplification. This is mainly the result of surface albedo feedbacks, reduced ice sheet cover and latitudinally dependent lapse rate feedbacks. The temperature differences are most pronounced where ice sheets are removed (including a strong elevation effect) and high latitude oceans, where sea ice cover is greatly reduced in all of the Pliocene cases. The Eoi^{400} climate shows an increased precipitation rate with respect to the E^{280} one. Both equatorial and high latitude regions are generally wetter in the Pliocene, while the sub-tropics become dryer (with a distinct poleward shift of the storm tracks). Particularly high precipitation amounts are seen over most of the Indian Ocean and its surroundings, owing to enhanced North African and South/Southeast Asian monsoons in the Pliocene.



535 The warmer Eoi⁴⁰⁰ climate with a reduced meridional temperature gradient compared to the pre-industrial reference agrees well with the available proxies. A strong Pliocene warming signal over the North Atlantic Ocean is seen in both the proxy record and our simulations, which can be linked to an enhanced AMOC. This stronger AMOC, however, is not linked to an overall increase in oceanic meridional heat transport. Moreover, the total (atmosphere + ocean) top of model induced meridional heat transport is slightly reduced in the warmer simulations, in line with the reduced meridional temperature gradient. The stronger and more variable AMOC in our Pliocene versus pre-industrial simulations can in part be explained by the altered vertical diffusivity parameter. Yet, it is mostly the result of the applied mid-Pliocene boundary conditions, in particular the closure of several Arctic gateways.

In addition to differences in the mean state between our Eoi⁴⁰⁰ and E²⁸⁰ cases, there are clear shifts in the different modes of variability studied here: ENSO, PMV and AMV. The ENSO amplitude is greatly reduced in our Pliocene simulations and characterised by shorter periodicity compared to the pre-industrial reference. The corresponding spatial pattern is also spread out across much of the tropical Pacific Ocean. Closely related to ENSO is the PMV in our E²⁸⁰ case, both having a distinct fingerprint on global SST variability on various time scales ranging from annual to multi-decadal. This teleconnection is lost in the Eoi⁴⁰⁰ case, with the PMV influence being mostly confined to just the North Pacific Ocean. Meanwhile, the AMV shows a strong connection to AMOC variability in our Pliocene simulations. Their mutual influence seems to be the dominant source of SST variability in the Eoi⁴⁰⁰, as opposed to ENSO/PMV in the E²⁸⁰.

As most of the PRISM4 boundary conditions, which are applied here as an external forcing to the model simulation, are in fact the result of long term feedbacks (i.e. ice melt and vegetation changes), the Eoi⁴⁰⁰ can serve as a good analog for future climatic changes. Our simulations show not only a strong warming compared to the pre-industrial reference, but also considerable regional changes and shifts in the dominant modes of variability.

Data availability. PlioMIP2 model data, including those of the simulations presented here, can be downloaded from the server located at the School of Earth and Environment of the University of Leeds. Contact Alan Haywood (a.m.haywood@leeds.ac.uk) for access. PlioMIP2 data from CESM2, EC-Earth3.3, NorESM1-F, IPSLCM6A and GISS2.1G can be obtained through the Earth System Grid Federation (ESGF) (<https://esgf-node.llnl.gov/search/cmip6/>, last access: 14 October 2021, ESGF, 2021).

560 *Author contributions.* MAK, MLJB, and ASvdH set up the model simulations, MAK and MLJB managed the simulations and post-processing of the data. MLJB performed the analyses and set up the manuscript. All authors contributed to the final shape and contents of the manuscript.

Competing interests. The authors declare to have no competing interests.



Acknowledgements. This work was carried out under the program of the Netherlands Earth System Science Centre (NESSC), financially supported by the Ministry of Education, Culture and Science (OCW, grant #024.002.001). Simulations were performed at the SURFsara dutch national computing facilities and were sponsored by NWO-EW (Netherlands Organisation for Scientific Research, Exact Sciences) under the projects 17189 and 2020.022.



References

- Baatsen, M., von der Heydt, A. S., Huber, M., Kliphuis, M. A., Bijl, P. K., Sluijs, A., and Dijkstra, H. A.: The middle to late Eocene greenhouse climate modelled using the CESM 1.0.5, *Climate of the Past*, 16, 2573–2597, <https://doi.org/10.5194/cp-16-2573-2020>, 2020.
- 570 Bellucci, A., Gualdi, S., and Navarra, A.: The double-ITCZ syndrome in coupled general circulation models: The role of large-scale vertical circulation regimes, *Journal of Climate*, 23, 1127–1145, <https://doi.org/10.1175/2009JCLI3002.1>, 2010.
- Bitz, C. M., Shell, K. M., Gent, P. R., Bailey, D. A., Danabasoglu, G., Armour, K. C., Holland, M. M., and Kiehl, J. T.: Climate sensitivity of the community climate system model, version 4, *Journal of Climate*, 25, 3053–3070, <https://doi.org/10.1175/JCLI-D-11-00290.1>, 2012.
- Blackmon, M., Boville, B., Bryan, F., Dickinson, R., Gent, P., Kiehl, J., Moritz, R., Randall, D., Shukla, J., Solomon, S., Bonan, G., Doney, S., Fung, I., Hack, J., Hunke, E., Hurrell, J., Kutzbach, J., Meehl, J., Otto-Bliesner, B., Saravanan, R., Schneider, E. K., Sloan, L., Spall, M., Taylor, K., Tribbia, J., and Washington, W.: The Community Climate System Model, *Bulletin of the American Meteorological Society*, 82, 2357–2376, [https://doi.org/10.1175/1520-0477\(2001\)082<2357:TCCSM>2.3.CO;2](https://doi.org/10.1175/1520-0477(2001)082<2357:TCCSM>2.3.CO;2), 2001.
- 575 Burke, K. D., Williams, J. W., Chandler, M. A., Haywood, A. M., Lunt, D. J., and Otto-Bliesner, B. L.: Pliocene and Eocene provide best analogs for near-future climates, *Proceedings of the National Academy of Sciences of the United States of America*, 115, 13 288–13 293, <https://doi.org/10.1073/pnas.1809600115>, 2018.
- 580 Danabasoglu, G., Ferrari, R., and McWilliams, J. C.: Sensitivity of an ocean general circulation model to a parameterization of near-surface eddy fluxes, *Journal of Climate*, 21, 1192–1208, <https://doi.org/10.1175/2007JCLI1508.1>, 2008.
- Danabasoglu, G., Bates, S. C., Briegleb, B. P., Jayne, S. R., Jochum, M., Large, W. G., Peacock, S., and Yeager, S. G.: The CCSM4 ocean component, *Journal of Climate*, 25, 1361–1389, <https://doi.org/10.1175/JCLI-D-11-00091.1>, 2012.
- 585 Deser, C., Phillips, A. S., Tomas, R. A., Okumura, Y. M., Alexander, M. A., Capotondi, A., Scott, J. D., Kwon, Y. O., and Ohba, M.: ENSO and pacific decadal variability in the community climate system model version 4, *Journal of Climate*, 25, 2622–2651, <https://doi.org/10.1175/JCLI-D-11-00301.1>, 2012.
- Dowsett, H., Robinson, M., Haywood, A., Salzmann, U., Hill, D., Sohl, L., Chandler, M., Williams, M., Foley, K., and Stoll, D.: The PRISM3D paleoenvironmental reconstruction, *Micropaleontology Press*, 2010.
- 590 Dowsett, H., Dolan, A., Rowley, D., Moucha, R., Forte, A. M., Mitrovica, J. X., Pound, M., Salzmann, U., Robinson, M., Chandler, M., Foley, K., and Haywood, A.: The PRISM4 (mid-Piacenzian) paleoenvironmental reconstruction, *Climate of the Past*, 12, 1519–1538, <https://doi.org/10.5194/cp-12-1519-2016>, 2016.
- Fetterer, F., Knowles, K., Meier, W., Savaoie, M., and Windnagel, K.: Sea ice index, version 3, <https://doi.org/10.7265/N5K072F8>, 2017.
- Foley, K. and Dowsett, H.: Community sourced mid-Piacenzian sea surface temperature (SST) data: U.S. Geological Survey data release, <https://doi.org/10.5066/P9YP3DTV>, 2019.
- 595 Gent, P. R. and McWilliams, J. C.: Isopycnal Mixing in Ocean Circulation Models, [https://doi.org/10.1175/1520-0485\(1990\)020<0150:MIOCM>2.0.CO;2](https://doi.org/10.1175/1520-0485(1990)020<0150:MIOCM>2.0.CO;2), 1990.
- Gent, P. R., Danabasoglu, G., Donner, L. J., Holland, M. M., Hunke, E. C., Jayne, S. R., Lawrence, D. M., Neale, R. B., Rasch, P. J., Vertenstein, M., Worley, P. H., Yang, Z. L., and Zhang, M.: The community climate system model version 4, *Journal of Climate*, 24, 4973–4991, <https://doi.org/10.1175/2011JCLI4083.1>, 2011.
- 600 Ghil, M., Allen, M. R., Dettinger, M. D., Ide, K., Kondrashov, D., Mann, M. E., Robertson, A. W., Saunders, A., Tian, Y., Varadi, F., and Yiou, P.: Advanced spectral methods for climatic time series, *Reviews of Geophysics*, 40, 3–1–3–41, <https://doi.org/10.1029/2000RG000092>, 2002.



- Gregory, J. M., Ingram, W. J., Palmer, M. A., Jones, G. S., Stott, P. A., Thorpe, R. B., Lowe, J. A., Johns, T. C., and
605 Williams, K. D.: A new method for diagnosing radiative forcing and climate sensitivity, *Geophysical Research Letters*, 31, 2–5,
<https://doi.org/10.1029/2003GL018747>, 2004.
- Haywood, A. M., Dolan, A. M., Pickering, S. J., Dowsett, H. J., McClymont, E. L., Prescott, C. L., Salzmann, U., Hill, D. J., Hunter,
S. J., Lunt, D. J., Pope, J. O., and Valdes, P. J.: On the identification of a pliocene time slice for data-model comparison, *Philosophical
Transactions of the Royal Society A: Mathematical, Physical and Engineering Sciences*, 371, <https://doi.org/10.1098/rsta.2012.0515>,
610 2013a.
- Haywood, A. M., Hill, D. J., Dolan, A. M., Otto-Bliesner, B. L., Bragg, F., Chan, W. L., Chandler, M. A., Contoux, C., Dowsett, H. J., Jost, A.,
Kamae, Y., Lohmann, G., Lunt, D. J., Abe-Ouchi, A., Pickering, S. J., Ramstein, G., Rosenbloom, N. A., Salzmann, U., Sohl, L., Stepanek,
C., Ueda, H., Yan, Q., and Zhang, Z.: Large-scale features of Pliocene climate: Results from the Pliocene Model Intercomparison Project,
Climate of the Past, 9, 191–209, <https://doi.org/10.5194/cp-9-191-2013>, 2013b.
- 615 Haywood, A. M., Dowsett, H. J., Dolan, A. M., Rowley, D., Abe-Ouchi, A., Otto-Bliesner, B., Chandler, M. A., Hunter, S. J., Lunt, D. J.,
Pound, M., and Salzmann, U.: The Pliocene Model Intercomparison Project (PlioMIP) Phase 2: Scientific objectives and experimental
design, *Climate of the Past*, 12, 663–675, <https://doi.org/10.5194/cp-12-663-2016>, 2016.
- Haywood, A. M., Tindall, J. C., Dowsett, H. J., Dolan, A. M., Foley, K. M., Hunter, S. J., Hill, D. J., Chan, W. L., Abe-Ouchi, A., Stepanek,
C., Lohmann, G., Chandan, D., Peltier, R. W., Tan, N., Contoux, C., Ramstein, G., Li, X., Zhang, Z., Guo, C., Nisancioglu, K. H., Zhang,
620 Q., Li, Q., Kamae, Y., Chandler, M. A., Sohl, L. E., Otto-Bliesner, B. L., Feng, R., Brady, E. C., von der Heydt, A. S., Baatsen, M. L.,
and Lunt, D. J.: The Pliocene Model Intercomparison Project Phase 2: Large-scale climate features and climate sensitivity, *Climate of the
Past*, 16, 2095–2123, <https://doi.org/10.5194/cp-16-2095-2020>, 2020.
- Herold, N., Buzan, J., Seton, M., Goldner, A., Green, J. a. M., Müller, R. D., Markwick, P., and Huber, M.: A suite of Early Eocene (~55
Ma) climate model boundary conditions, *Geoscientific Model Development*, 7, 2077– 2090, <https://doi.org/10.5194/gmd-7-2077-2014>,
625 www.geosci-model-dev.net/7/2077/2014/, 2014.
- Huang, B., Thorne, P. W., Banzon, V. F., Boyer, T., Chepurin, G., Lawrimore, J. H., Menne, M. J., Smith, T. M., Vose, R. S., and Zhang,
H. M.: Extended reconstructed Sea surface temperature, Version 5 (ERSSTv5): Upgrades, validations, and intercomparisons, *Journal of
Climate*, 30, 8179–8205, <https://doi.org/10.1175/JCLI-D-16-0836.1>, 2017.
- Hunke, E. C. and Lipscomb, W. H.: The Los Alamos sea ice model, documentation and software., Tech. Rep. LA-CC-06-012, version 4.,
630 2008.
- Hurrell, J. W., Holland, M. M., Gent, P. R., Ghan, S., Kay, J. E., Kushner, P. J., Lamarque, J. F., Large, W. G., Lawrence, D., Lindsay, K.,
Lipscomb, W. H., Long, M. C., Mahowald, N., Marsh, D. R., Neale, R. B., Rasch, P., Vavrus, S., Vertenstein, M., Bader, D., Collins,
W. D., Hack, J. J., Kiehl, J., and Marshall, S.: The community earth system model: A framework for collaborative research, *Bulletin of
the American Meteorological Society*, 94, 1339–1360, <https://doi.org/10.1175/BAMS-D-12-00121.1>, 2013.
- 635 Kiehl, J. T., Shields, C. A., Hack, J. J., and Collins, W. D.: The climate sensitivity of the Community Climate System Model ver-
sion 3 (CCSM3), *Journal of Climate*, 19, 2584–2596, <https://doi.org/10.1175/JCLI3747.1>, [https://journals.ametsoc.org/doi/full/10.1175/
JCLI3747.1](https://journals.ametsoc.org/doi/full/10.1175/JCLI3747.1), 2006.
- Large, W. G., McWilliams, J. C., and Doney, S. C.: Oceanic Vertical Mixing - a Review and a Model with a Nonlocal Boundary-Layer
Parameterization, *Reviews of Geophysics*, 32, 363–403, <https://doi.org/10.1029/94rg01872>, 1994.
- 640 Lawrence, D. M., Oleson, K. W., Flanner, M. G., Thornton, P. E., Swenson, S. C., Lawrence, P. J., Zeng, X., Yang, Z.-L., Levis, S., Sakaguchi,
K., Bonan, G. B., and Slater, A. G.: Parameterization improvements and functional and structural advances in Version 4 of the Community



- Land Model, *Journal of Advances in Modeling Earth Systems*, 3, <https://doi.org/10.1029/2011MS00045>, <http://doi.wiley.com/10.1029/2011MS00045>, 2011.
- 645 Loptson, C. A., Lunt, D. J., and Francis, J. E.: Investigating vegetation-climate feedbacks during the early Eocene, *Climate of the Past*, 10, 419–436, <https://doi.org/10.5194/cp-10-419-2014>, 2014.
- McClymont, E. L., Ford, H. L., Ling Ho, S., Tindall, J. C., Haywood, A. M., Alonso-Garcia, M., Bailey, I., Berke, M. A., Littler, K., Patterson, M. O., Petrick, B., Peterse, F., Christina Ravelo, A., Risebrobakken, B., De Schepper, S., Swann, G. E., Thirumalai, K., Tierney, J. E., van der Weijst, C., White, S., Abe-Ouchi, A., Baatsen, M. L., Brady, E. C., Chan, W. L., Chandan, D., Feng, R., Guo, C., von der Heydt, A. S., Hunter, S., Li, X., Lohmann, G., Nisancioglu, K. H., Otto-Bliesner, B. L., Peltier, R. W., Stepanek, C., and Zhang, Z.: Lessons from
650 a high-CO₂ world: An ocean view from ~3 million years ago, *Climate of the Past*, 16, 1599–1615, <https://doi.org/10.5194/cp-16-1599-2020>, 2020.
- Neale, R. B., Richter, J., Park, S., Lauritzen, P. H., Vavrus, S. J., Rasch, P. J., and Zhang, M.: The Mean Climate of the Community Atmosphere Model (CAM4) in Forced SST and Fully Coupled Experiments, *Journal of Climate*, 26, 5150–5168, <https://doi.org/10.1175/JCLI-D-12-00236.1>, 2013.
- 655 Oldeman, A. M., Baatsen, M. L. J., von der Heydt, A. S., Haywood, A. M., Booth, A., Hunter, S. J., Chan, W.-L., Abe-Ouchi, A., Stepanek, C., Lohmann, G., Chandan, D., Peltier, W. R., Tan, N., Contoux, C., Ramstein, G., Li, X., Zhang, Z., Guo, C., Nisancioglu, K. H., Zhang, Q., Li, Q., Kamae, Y., Chandler, M. A., Sohl, L. E., Feng, R., Otto-Bliesner, B. L., Brady, E. C., Lunt, D. J., Williams, C., Pontes, G. M., and Wainer, I.: Reduced El-Niño variability in the mid-Pliocene according to the PlioMIP2 ensemble, *Climate of the Past Discussions*, 2021.
- 660 Oleson, K. W., Lawrence, D. M., Gordon, B., Flanner, M. G., Kluzek, E., Peter, J., Levis, S., Swenson, S. C., Thornton, E., Dai, A., Decker, M., Dickinson, R., Feddes, J., Heald, C. L., Lamarque, J.-f., Niu, G.-y., Qian, T., Running, S., Sakaguchi, K., Slater, A., Stöckli, R., Wang, A., Yang, L., Zeng, X., and Zeng, X.: Technical Description of version 4.0 of the Community Land Model (CLM), NCAR Tech. Note, NCAR/TN-47, 2010.
- Peng, G., Meier, W. N., Scott, D. J., and Savoie, M. H.: A long-term and reproducible passive microwave sea ice concentration data record
665 for climate studies and monitoring, *Earth System Science Data*, 5, 311–318, <https://doi.org/10.5194/essd-5-311-2013>, 2013.
- Rosenbloom, N. A., Otto-Bliesner, B. L., Brady, E. C., and Lawrence, P. J.: Simulating the mid-Pliocene Warm Period with the CCSM4 model, *Geoscientific Model Development*, 6, 549–561, <https://doi.org/10.5194/gmd-6-549-2013>, <http://www.geosci-model-dev.net/6/549/2013/>, 2013.
- Smith, R. D. and McWilliams, J. C.: Anisotropic horizontal viscosity for ocean models, *Ocean Modelling*, 5, 129–156,
670 [https://doi.org/10.1016/S1463-5003\(02\)00016-1](https://doi.org/10.1016/S1463-5003(02)00016-1), 2003.
- Smith, R. D., Jones, P., Briegleb, B., Bryan, F., Danabasoglu, G., Dennis, J., Dukowicz, J., Eden, C., Fox-Kemper, B., Gent, P., Hecht, M., Jayne, S., Jochum, M., Large, W., Lindsay, K., Maltrud, M., Norton, N., Peacock, S., Vertenstein, M., and Yeager, S.: The Parallel Ocean Program (POP) reference manual: Ocean component of the Community Climate System Model (CCSM), Los Alamos National Laboratory Tech. Rep. LAUR-10-01853, 141, 1–141, www.cesm.ucar.edu/models/cesm1.0/pop2/doc/sci/POPRefManual.pdf, 2010.
- 675 Steele, M., Morley, R., and Ermold, W.: PHC: A global ocean hydrography with a high-quality Arctic Ocean, *Journal of Climate*, 14, 2079–2087, [https://doi.org/10.1175/1520-0442\(2001\)014<2079:PAGOHW>2.0.CO;2](https://doi.org/10.1175/1520-0442(2001)014<2079:PAGOHW>2.0.CO;2), 2001.
- Trenberth, K. E. and Shea, D. J.: Atlantic hurricanes and natural variability in 2005, *Geophysical Research Letters*, 33, 1–4, <https://doi.org/10.1029/2006GL026894>, 2006.